Calhoun
Institutional Archive of the Naval Postgraduate School

Calhoun: The NPS Institutional Archive

DSpace Repository

Theses and Dissertations | 1. Thesis and Dissertation Collection, all items

2001

Effects of precipitate size and surface normal orientation on micro-identification and compressive fatigue of NiTi shape memory alloys

Juntunen, Kevin K.

Monterey California. Naval Postgraduate School

http://hdl.handle.net/10945/24340

This publication is a work of the U.S. Government as defined in Title 17, United States Code, Section 101. Copyright protection is not available for this work in the United States.

Downloaded from NPS Archive: Calhoun

http://www.nps.edu/library

Calhoun is the Naval Postgraduate School's public access digital repository for research materials and institutional publications created by the NPS community. Calhoun is named for Professor of Mathematics Guy K. Calhoun, NPS's first appointed -- and published -- scholarly author.

Dudley Knox Library / Naval Postgraduate School
411 Dyer Road / 1 University Circle
Monterey, California USA 93943

EFFECTS OF PRECIPITATE SIZE AND SURFACE NORMAL ORIENTATION ON MICRO-INDENTATION AND COMPRESSIVE FATIGUE OF NiTi SHAPE MEMORY ALLOYS

by

KEVIN K. JUNTUNEN

B.S., Illinois Institute of Technology, 1993

A thesis submitted to the Faculty of the

Graduate School of the University of Colorado at

Boulder in partial fulfillment of the requirements

for the degree of Master of Science

Department of Mechanical Engineering

2001

DISTRIBUTION STATEMENT A
Approved for Public Release
Distribution Unlimited

20010816 034

AQM01-10-2252

This thesis entitled:

Effects of Precipitate Size and Surface Normal Orientation on the Micro-Indentation and Compressive Fatigue of NiTi Shape Memory Alloys

written by Kevin K. Juntunen

has been approved for the Department of Mechanical Engineering

_____

Kenneth A. Gall

_____

Rishi Raj

_____

Martin L. Dunn

Date_____

The final copy of the thesis has been examined by the signatories, and we find that both the content and the form meet acceptable presentation standards of scholarly work in the above mentioned discipline.

Juntunen, Kevin K. (MS, Mechanical Engineering)

Effects of Precipitate Size and Surface Normal Orientation on the Micro-Indentation and Compressive Fatigue of NiTi Shape Memory Alloys

Thesis directed by Assistant Professor Kenneth Allen Gall

Abstract

This work seeks to determine the evolution of the indentation and fatigue response of heat-treated Nickel-Titanium shape memory alloys over a range of precipitate sizes and surface normal orientations. Various tests were used to determine the impact of aging treatments on particle size, coherence, and phase transition temperatures. Through instrumented sharp microindentation and cyclic compression testing, the varying mechanical response of the NiTi materials given different aging treatments was determined. Small precipitate sizes were found to strongly resist dislocation motion and the martensitic transformation. Intermediate precipitate sizes had lower resistance to both mechanisms. For the larger precipitates, the resistance to dislocation motion continued to lessen, while the resistance to martensitic transformation increased. During indentation, the [100] orientation tended to exhibit the greatest resistance to dislocation motion, while [221] showed the least. An orientation dependence of resistance to transformation was not obvious in the indentation tests. Cyclic compression tests showed that orientation and heat treatment combinations that resisted dislocation motion while allowing martensitic transformation showed the least residual strain

accumulation and cyclic degradation. Those specimens that resisted the transformation or allowed significant dislocation motion saw a considerable reduction in the compressive hysteresis over 100 cycles.

Acknowledgements

Mark Stavig of Sandia National Laboratory, Mark Polinsky of Memry Corporation, and Stephen Kelley of the National Renewable Energy Laboratory (NREL) all provided Differential Scanning Calorimetry testing for the various specimens.

Hans J. Maier and A. Lershe of the University of Paderborn, Germany provided Transmission Electron Microscope (TEM) images and Diffraction Pattern Analysis, as well as valuable insight into interpreting the results.

This work is the progression of previous work by my advisor, Ken A. Gall. His assistance in conducting and understanding the experiments related to this thesis was indispensable, and I greatly appreciate his help with various aspects of my continuing education.

TABLE OF CONTENTS

1. BACKGROUND 1
- 1.1 Nickel-Titanium Shape Memory Alloys 1
- 1.2 Proposed Mechanical Testing 4
- 1.3 State of Current Research 6
- 1.4 Scope of this Study 7

2. METHODOLOGY 9
- 2.1 Specimens and Specimen Preparation 9
- 2.2 Instrumented Sharp Micro-Indentation 13
- 2.3 Cyclic Loading in Compression 17
- 2.4 Secondary Tests 18

3. RESULTS 20
- 3.1 TEM Imaging 20
- 3.2 Diffraction Pattern Analysis 22
- 3.3 Differential Scanning Calorimetry 23
- 3.4 Hardness Testing 24
- 3.5 Elastic Recoverability 29
- 3.6 Cyclic Response to Compression 29

4. DISCUSSION 36
- 4.1 Evolution of Hardness with Increasing Precipitate Size 36
- 4.2 Evolution of Elastic Recoverability with Increasing Precipitate Size 37
- 4.3 Orientation Effects 38
- 4.4 Dislocation Activity 41
- 4.5 Stress-induced Martensitic Transformation 44
- 4.6 Evolution of Cyclic Compressive Response with Increasing Precipitate Size 46
- 4.7 Statistical Analysis 48

5. CONCLUSIONS 51

6. REFERENCES 53

TABLES

Table 1: Apparent precipitate sizes for five aging temperatures 20

Table 2: Average hardness values (in GPa) for ten indentations 25

Table 3: Average elastic recoverability (in percent) for ten indentations 29

Table 4: Maximum stresses experienced in first compressive cycle 39

Table 5: Two-factor analysis of variance with replication for measured hardness values 48

Table 6: Two-factor analysis of variance with replication for elastic recoverability 49

FIGURES

Figure 1: An example load-depth curve with annotated areas of interest 16

Figure 2: Determination of transition temperatures 18

Figure 3: Precipitates observed in aging temperature of 623 K 21

Figure 4: Precipitates observed in aging temperature of 673 K 21

Figure 5: Precipitates observed in aging temperature of 723 K 21

Figure 6: Precipitates observed in aging temperature of 773 K 21

Figure 7: Precipitates observed in aging temperature of 823 K 21

Figures 8-10: Increasing magnification views of an area showing combined martensite transformation and dislocation activity 22

Figure 11: Diffraction pattern analysis for aging temperature of 673 K 23

Figure 12: Diffraction pattern analysis for aging temperature of 723 K 23

Figure 13: Diffraction pattern analysis for aging temperature of 773 K 23

Figure 14: Combined Differential Scanning Calorimetry results 24

Figure 15: Loading curves for the [100] orientation 25

Figure 16: Loading curves for the [110] orientation 26

Figure 17: Loading curves for the [111] orientation 26

Figure 18: Loading curves for the [210] orientation 27

Figure 19: Loading curves for the [221] orientation 27

Figure 20: Loading curves for the [221] orientation 28

Figure 21: Loading curves for the [321] orientation 28

Figure 22: Compressive response of [210] oriented Solutionized NiTi 30

Figure 23: Compressive response of [210] oriented NiTi aged at 623 K 30

Figure 24: Compressive response of [210] oriented NiTi aged at 673 K 31

Figure 25: Compressive response of [210] oriented NiTi aged at 823 K 31

Figure 26: Compressive response of [100] oriented Solutionized NiTi 32

Figure 27: Compressive response of [100] oriented NiTi aged at 673 K 32

Figure 28: Compressive response of [100] oriented NiTi aged at 823 K 33

Figure 29: Compressive response of [111] oriented Solutionized NiTi 33

Figure 30: Compressive response of [111] oriented NiTi aged at 623 K 34

Figure 31: Compressive response of [111] oriented NiTi aged at 673 K 34

Figure 32: Compressive response of [111] oriented NiTi aged at 823 K 35

Figure 33: Hardness vs. precipitate size 36

Figure 34: Recoverable energy vs precipitate size 37

Figure 35: Residual strain accumulation for solutionized [100], [210], and [111] specimens 39

Figure 36: Stereographic triangle depicting Schmidt factors associated with transformation stresses for varying orientations 40

Figure 37: Stereographic triangles depicting Schmidt factors associated with plastic strain for varying orientations 42

Figure 38: Residual strain accumulation for the [210] orientation 47

Figure 39: Combined Hardness and Elastic Recoverability for all orientations 52

1. Background

1.1 Nickel-Titanium Shape Memory Alloys

Shape memory alloys are materials that can experience considerable amounts of strain and return to their original shape. Depending upon the needs of the application, this effect can be tailored to be either instantaneous or dependent upon thermal activation. The potential applications for the properties of shape memory alloys are promising. Established applications for medical implants, orthodontics, hydraulic pipe couplings, and actuators have demonstrated that the industrial utilization of shape memory materials is feasible (Brailovski and Trochu, 1996; Otsuka and Wayman, 1998). Their usage in microelectromechanical systems (Johnson, 1999) and smart civil structures has been proposed for future applications.

The characteristic that makes shape memory alloys notable is the unique ability to deform through a reversible mechanism known as a martensitic transformation. This transformation is diffusionless and entails an alteration of the crystallographic structure of the original material through a coordinated shearing mechanism. Near-equiatomic NiTi has a parent phase organized in a cubic B2 structure. Martensitic transformation converts this to a monoclinic B19′ phase. Certain microstructures will also favor an intermediate transformation to a trigonal R phase. Although the R phase transformation is also a martensitic one, the associated strains are of a much smaller order. It is

the transformation to the B19' phase that is of primary interest, as it accounts for the bulk of the strains utilized in shape memory applications.

The driving force for the transformation is governed by solution thermodynamics. The Gibb's free energy of the substance determines the stable phase. Two main factors can induce transformation when it is not favored: stress and temperature. In stress-induced transformations, applied stresses introduce strain energy into the lattice, which can overcome the barrier to transformation. In temperature-induced transformations, the Gibb's free energy of the material in the martensite phase falls below that of the parent phase (B2 intermetallic for NiTi) with decreasing temperature. When the difference in free energy between the parent and martensite reaches a critical value, a phase transformation is thermodynamically favored to reduce the energy of the system. When the conditions that imposed the transformation are removed, equal and opposite factors drive a reverse transformation to the parent phase. However, if the final state lies between the austenite and martensite transformation points, the driving force will not be sufficient to induce reverse transformation (Otsuka and Wayman, 1998).

In the absence of an applied stress, these transformations will occur at set temperatures. Four temperatures characterize the martensitic transformation and the reverse transformation. As a specimen of homogeneous austenite composition is cooled, at some point it will begin to transform to martensite. This is referred to as the martensite start temperature. With continued cooling, the specimen will

completely transform at a point referred to as the martensite finish temperature. Upon reheating, analogous points for the reverse transformation, known as the austenite start and finish temperatures, can be determined. The differential scanning calorimetry tests used in this work utilize cooling and heating cycles to determine these temperatures by detecting the transfer of an associated heat of transformation.

For cases where the material experiences reverse transformation immediately upon unloading, this phenomenon is referred to as pseudoelasticity. In cases where the driving force is insufficient to induce reverse transformation upon removal of an applied stress, elevating the temperature of the material will increase the driving force until transformation begins at the austentite start temperature. This phenomenon is known as the shape memory effect. In either case, the process is analogous to normal elastic response, but with considerably greater strain ranges than those of conventional metals (3-6% for NiTi alloys).

The transformation is not entirely reversible in practice. Studies (Sehitoglu et al., 2000 and Gil et al., 1996) have demonstrated that residual strains remain after uniaxial loading below levels that induce macroscale plastic flow and that the stress required to induce transformation reduces with each cycle. One possible explanation put forth is that microscale dislocation motion at low stress levels can block the reverse transformation and stabilize small sections of martensite. This behavior has significant implications for applications such as

actuators, since the conditions that activate the transformation can change incrementally with each cycle.

For these materials to be used to their full potential in a wide range of applications, a robust means of characterization is required to predict how the material will respond in service and how different treatments can tailor material properties to engineering needs.

1.2 Proposed Mechanical Testing

Indentation has long been used as a means to directly measure the hardness of a material. Using a known load, the hardness can be determined from either the rebound height of the indenter or the final depth of penetration. Instrumented indentation improves on this method. An indenter of known geometry penetrates the material while controlling the either the rate of load application or the indenter depth. At regular intervals of the controlled parameter, the other parameter is recorded. With such a record of the evolution of the material's response, more detailed information can be gathered, such as Young's modulus, strain hardening exponents, and fracture toughness (Giannakopoulos and Suresh, 1999). All instrumented indentation tests in this work will use a diamond-shaped Vicker's, or sharp, indenter. They will also exclusively use microindentation, where the indenter is very small, loads are on the order of milliNewtons, and depths are on the order of micrometers. In such tests, great care must be given to ensure an adequate surface preparation, as surface effects can greatly influence the test results.

Instrumented sharp microindentation has been proposed as a promising method of determining elastoplastic properties of materials. Although difficulties do arise in interpreting the results arising from how the material responds to indentation (e.g.: "sink-in" or "pile-up" of material around the indentation affecting the projected area of indentation), its superior utility in small-scale applications and applications where spatial microstructural variations exist make it a promising candidate for some of the nascent NiTi applications. It also enjoys the benefits of being non-destructive, performable at varying points on a sample, and capable of delivering information on many of the properties that are of interest in mechanical design (Oliver and Pharr, 1992; Giannakopoulos and Suresh, 1999).

Cyclic compression testing is of interest because it is considerably more analogous to the macroscopic loading regimes these materials experience in real world applications. Subjecting the specimens to repeated uniaxial compressive stresses and analyzing the stress-strain curves over several cycles quantifies the build up of residual stresses and the degradation of the martensitic transformation. Comparing the results across different aging treatments and surface normal orientations highlights the effects of these factors on the overall response.

1.3 State of Current Research

The field of mechanical characterization of NiTi shape memory alloys is still a developing one, and new studies are constantly being published which bring us incrementally closer to a complete understanding of these materials. Many of these present macroscale experimental results on polycrystalline NiTi, with little insight given into the mechanisms occurring or the evolution of the response to changes in material composition or structure. In particular, the scope of existing research into instrumented sharp indentation of NiTi shape memory alloys to date has been limited.

There have been numerous studies performed on the mechanical response of NiTi shape memory alloys through various methods. Three in particular are of interest, and this work is a progression of those studies. The response to compressive stress of similar single crystal specimens with an emphasis on the effects of orientation, peak-aging, and overaging demonstrated the effect of these microstructural variations on mechanical response (Sehitoglu et al., 2000). A related study examined the effect of similar microstructural effects on the cyclic compressive response. (Sehitoglu et al., 2001). The final of these three studies looks at the orientation dependence of the response of solutionized single crystal NiTi to both macroscale compressive stresses and instrumented sharp microindentation (Gall et al., 2000). Absent from any of these is an examination of the response across a wide range of aging treatments and orientations.

Existing studies containing indentation results have examined: the pseudoelasticity of an undetermined as-received alloy to as-received specimens subjected to a single, mild heat treatment (Liu et al., 1999), indentation response to varying orientations in single-crystal solutionized specimens (Gall et al., 2000), and raw test results from extremely mild and strong heat treatments (Gil et al., 1996). Another work takes a detailed look at the effect of variations in microstructure through heat-treatment, cold-work, and annealing, but is focused on the implications for transition temperatures and does not examine the connection to mechanical response in any detail (Treppman et al., 1995). Therefore, although studies have been published on the response of NiTi to instrumented sharp indentation, a comprehensive examination of the topic has yet to emerge.

1.4 Scope of this Study

This work seeks to undertake a comprehensive study of the evolution of the mechanical response across a full range of aging treatments and orientations and to determine the mechanisms that influence the compression and indentation response. To accomplish this, the following testing procedure is proposed:

- TEM imaging will be used to gain visual insights into the mechanisms of the response and to evaluate the effect of varying aging treatments on precipitate size.

- Diffraction pattern analysis will be used to determine the degree to which the differently sized precipitates remain coherent with the parent matrix (i.e.: there is a degree of continuity in the lattice structure across the precipitate-matrix interface)
- Differential scanning calorimetry will be used to determine the transformation temperatures for each aging treatment.
- Instrumented sharp indentation will provide values of hardness and elastic recoverability across the full range of aging treatments.
- Repeated compression tests will demonstrate the evolution of the stress-strain response during cyclic loading across the full range of aging treatments.

The combined results of these tests will be analyzed as a whole to determine the effects of aging on the mechanical response of the material. It is hoped that this will provide a stimulus for the development of a robust means of characterizing the anticipated mechanical response of NiTi shape memory alloys and will lead to a better understanding of how aging treatments can help tailor the properties of these materials for their intended use.

2. Methodology

2.1 Specimens and Specimen Preparation

This research uses specimens of a single composition: near-equiatomic Nickel-Titanium (50.9at% Ti). All specimens are single crystals grown through the modified Bridgeman Technique in an inert gas atmosphere. All specimens were cut from the same bulk sample using Electro-Discharge Machining (EDM). They are grouped in seven different measured crystallographic orientations from the surface normal vector: [100], [110], [111], [210], [211], [221], and [321]. As differently oriented specimens are indistinct from each other, careful organization was required to prevent indiscriminately mixing them together. All specimens were approximately 4mm x 4mm x 7mm.

Specimens were etched in a solution of $3HNO_3 + 2H_2O + HF$ under a fume hood to remove the surface oxide coating and prevent its partial diffusion into the metal during aging. The resulting waste was disposed through the University's Environmental and Health Services Department. Etching in this manner produced extremely variable results between different specimens. For some specimens, the coating material rapidly dissolved away, leaving a white metal finish still bearing machining marks from the cutting process. Others experienced no visible removal after prolonged exposure. Still others showed both tendencies, and these were the most problematic. In such cases, stubborn portions of the coating remained unaffected, while the remaining surface was exposed metal. Since the etchant reacts considerably stronger to the metal than the

coating, prolonged exposure in such cases tended to deform the specimen geometry beyond acceptable limits. In either of the latter two cases, the specimens were removed from the etchant, and the remaining coating was removed through mechanical grinding and polishing.

The samples were then aged for a constant 90 minutes at temperatures of 623 K, 673 K, 723 K, 773 K, and 823 K in a high temperature oven. Prior to aging, I calibrated a thermocouple, then tested the oven's ability to hold a steady temperature over time at the exact location I intended to age the samples. These tests demonstrated that: after a roughly half-hour stabilization period, the oven could hold the set temperature to within a degree Kelvin; and the measured temperatures at the intended aging location lagged behind the oven's readout temperature during said stabilization. I then aged the specimens in five batches, each batch containing two specimens from each of the seven orientations and an additional three specimens of unknown orientation for associated testing to be discussed later. Specimens were aged on an aluminum tray bent accordion style to prevent mixing different orientations together. Following the ninety-minute exposure time at each temperature, they were removed and rapidly quenched in room temperature water. An interesting though inconsequential effect of the aging process was the formation of an oxide coating that varied greatly in color with increasing temperature. After aging at 623 K, the sampled were covered in a golden tinged oxide. After aging at 673 K, the oxide was still mostly golden, but flecked with spots of red. Aging at 723

K produced a bluish tinge with red and violet spotting. Aging at 773 K produced a light blue tinge. The last aging temperature, 823 K, produced a blackish tinge with rainbow hues throughout.

The aged specimens were then mounted in quick-setting acrylic sample molds. Each mold contained one specimen of each aging temperature from the same crystallographic orientation. As I prepared two samples for each combination of orientation and aging temperature, each orientation had two sample molds prepared for it. Prior to placing in the molds, each specimen was labeled with a marker to provide a means to identifying individual specimens within the mold and after the mold was broken.

These acrylic sample molds containing the specimens were then sanded using sandpaper of increasing grit (240, 320, 480, and 600 grit) on a Buehler Handimet. After each course of sanding, the surface was carefully inspected to ensure that the deeper gouges characteristic of artifacts of previous sanding had been removed, and the top and bottom surfaces were checked to ensure they were roughly parallel. The specimen was then thoroughly washed to prevent contaminating the sandpaper with higher grit particles. Following sanding, the molds were polished on a rotating plate saturated with diamond pastes of decreasing particle size (15, 6, 1 and _ micron). In between courses, the samples were measured with calipers to ensure that a depth equal to at least three times the diameter of the prior course's abrasive particles was removed. The molds were again washed to prevent particle contamination from

larger abrasives. All of this surface preparation was performed to ensure that the surface roughness was reduced to a point where it would no longer influence the indentation response.

At this point, I examined the prepared specimen surfaces under a microscope. I discovered that, probably due to the variation in hardness of the different specimens in the molds, that some specimens contained unacceptable levels of surface roughness, while other specimens in the molds were acceptable. I increased the polishing time for each grit and analyzed the results until I found a suitable procedure, then performed this on all sample molds.

From the remaining aged "dummy" specimens, I cut four 2mm x 2mm x 4mm pieces with a diamond saw for later DSC testing. Due to the extreme hardness of NiTi, this turned out to be a quite lengthy process. The remnants of each cut sample were also collected for TEM imaging and Diffraction Pattern Analysis.

The sample molds were finished around the time when the initial DSC results were received. After analysis of the parent and martensite transition temperatures, it became clear that room temperature was between the two transition start temperatures for some aging temperatures. In these cases, specimens exposed to sufficiently low temperatures to induce martensite would not reverse transform at room temperature, and I could not be absolutely certain that this had not happened. Therefore, I performed a final preparation step of heating the samples at 350 K for 30 minutes to ensure a homogeneous composition of

austenite and stored the samples at room temperature thereafter. This completed the preparation for indentation, and such tests were performed.

Following completion of the indentation tests, the specimens were cut from their molds. Although each specimen had one finely polished end already, both ends required polishing to reduce barreling effects from friction in the cyclic compression tests. Such polishing was performed prior to these tests, and the specimens were again heated to ensure a uniform composition of austenite.

2.2 Instrumented Sharp Micro-indentation

I performed all of the hardness tests using a Fisherscope-H100 micro hardness testing machine (Fisherscope). Tests were performed at room temperature under load control conditions. The indenter used in all tests was a diamond Vicker's indenter with a 136° face angle. The applied loading and unloading rate was 100 microNewtons (mN) per second to a maximum of 1000 mN. Each individual micro hardness test took twenty seconds, and required an average two minutes of set-up time. The respective load and depth measuring resolutions for the Fisherscope are +/- 0.02 mN and +/- 2 nm.

To perform each test, I first viewed the specimen surface through the Fisherscope's microscope to locate a suitable area for indentation. Due to the relative softness of the acrylic molds, it wore at a much faster rate than the NiTi during surface preparation. This caused the NiTi

specimen surfaces to stick out above the surface of the mold, and the edges of the specimens to be rounded off. The area around these edges was therefore not prepared as well as the interior portions of the surface. I ensured that indentations were performed some distance from these edges, but in a manner consistent with a degree of spatial variation across the surface. I also ensured that individual indentations were performed at a considerable distance from previous tests to prevent possible deformation zone effects.

After selection of an adequate testing area, the mold was shifted to the area under the indenter and the indenter housing was lowered on to the specimen. After the housing contacted the specimen surface, the housing was manually adjusted to parallel, then the test was initiated. Once the test was complete, I moved the specimen back under the microscope viewer. As the actual location of the indentation would unpredictably fall outside of the designated crosshairs superimposed on the microscope viewer, a suitability check had to be performed after indentation also to ensure that the actual indentation fell within an acceptable area. I would also check the indentation for sink-in, pile-up, surrounding slip bands, or any other distinct features.

Initially, I performed fifteen indentations on five solutionized [210] specimens to determine the variability in the test. This data indicated that 10 indentations per orientation-heat treatment combination would be sufficient for statistical significance at a 95% confidence level. Eighty-four specimens were indented five times each for a total of 420

indentations. This data was later subjected to an analysis of variance to determine how well the statistics of the initial sample held up over the entire population of specimens, and these results will be discussed later in chapter 4.4.

The Fisherscope outputted raw data from each indentation in 200 load-depth pairings. The resulting 200 pairings were exported to a spreadsheet and graphed. The hardness values were determined from (x,y) pairings of load and depth. Knowing the geometry of the indenter, the projected area that directly resists indentation can be derived as a function of depth. The applied load divided by the resulting projected area yields a value in units of stress that is used to indicate hardness. The exact formula I used was:

$$H_v \text{ (Gpa)} = \frac{\text{Load (mN)}}{\{24.5 \times [\text{depth } (\mu\text{m})]^2\}}$$

(Giannakopoulos et al., 1994). These values were calculated at 100 mN, 500 mN, and 1000 mN. Smaller values of load tended to result in higher values of hardness, but this converged to a relatively constant value at 1000 mN. This is a commonly observed phenomenon caused by both size effect (the tendency for a smaller sample region to have fewer defects) and the geometry of the indenter (the tip cannot be infinitely sharp). Observing the evolution of the hardness response for increasing loads and assuring convergence allows me to discount size effect as a major variable in the response. For comparative purposes, only calculated hardness values at 1000 mN will be used.

The percentage of recoverability of the deformation was also tabulated. The depth at which the unloading curve crosses the Y-axis gives us a measure of the amount of recovered deformation, but a better indication is to find the ratio between the areas under the two curves (taken from the Y-axis). This ratio calculates the percentage of work required to cause the deformation that can be recovered upon unloading, and is the measurement of elastic recoverability that I will use in this paper. For each indentation performed, the Fisherscope directly calculated this value. Figure 1 shows a typical load-depth curve and the associated data drawn from it.

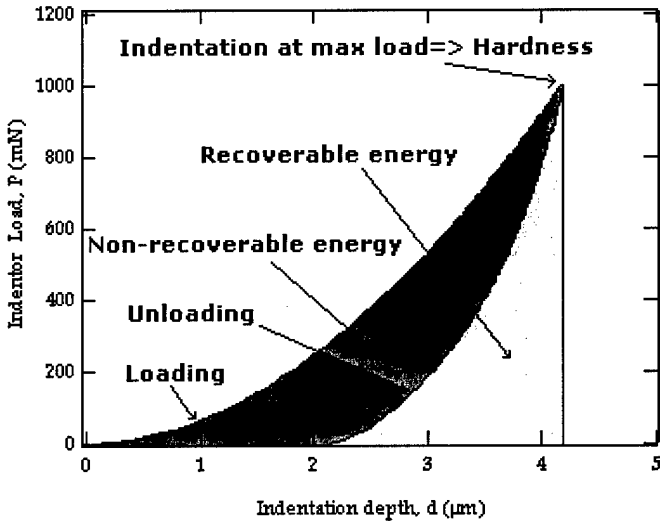

Figure 1: An example load-depth curve with annotated areas of interest.

This curve demonstrates the uniqueness of shape memory alloys. If the response was purely elastic, the loading and unloading curves would be the same. A traditional metallic material would exhibit more plasticity, which would be manifested as a more vertical unloading curve.

From all this data, combined graphs were made depicting the trends in response for varying aging temperatures and orientations.

2.3 Cyclic Loading in Compression

Cyclic compression tests were performed with an Instron servo-hydraulic load frame. Bars with parallel ends were placed in the grips of the Instron, and the specimen was placed between these. The tests were performed in strain control for the loading portion of the cycle and in load control for the unloading portion. In strain controlled loading, the system continuously applies greater loads until a target value for strain is reached. In load controlled unloading, the system steadily reduced the applied load to a pre-determined minimum necessary to hold the specimen in place. Strain control was inappropriate for unloading as the residual strains that accumulated on each cycle would cause the bars of the test machine to lose contact with the specimen at the end of unloading. Strain was measured through an extensiometer, calibrated and pressed firmly against the specimen with latex bands. A pre-set program would then perform compression loading over 100 cycles up to a -3% applied strain. Although accumulated residual strains reduced the total strain range, the upper bound strain value remained constant over all 100 cycles. This procedure was performed for the [100], [111], and [210] orientations and limited to the 623 K, 673 K, and 823 K heat treatments and solutionized specimens. All tests were performed at room temperature.

The dimensions of each specimen were entered into the Instron's test program prior to the test, and the results were outputted in (x,y) pairings of stress and strain. These values were exported to a spreadsheet, graphed for each cycle, and the evolution of the response over multiple cycles was examined. Compressive stress and strain values were made positive to facilitate graph reading.

2.4 Auxiliary Tests

As previously acknowledged, DSC testing was performed with the help of three individuals: Mark Stavig of Sandia National Laboratory, Mark Polinsky of Memry Corporation, and Stephen Kelley of the National Renewable Energy Laboratory (NREL). A Perkin-Elmer Differential Scanning Calorimeter was used to perform these tests on specimens from each aging temperature. The specimens were initially held at 293 K for one minute, then cooled to 203 K at a rate of 10 K/minute. After being held at 203 K for two minutes, they were then raised to 423 K at the same rate. After two minutes at 423 K, they were then cooled again to 203 K at 10 K/minute. After graphing temperature against heat transferred, the transformation temperatures were calculated from the observed spikes in heat transfer using the intersection of average slope lines as shown in figure 2.

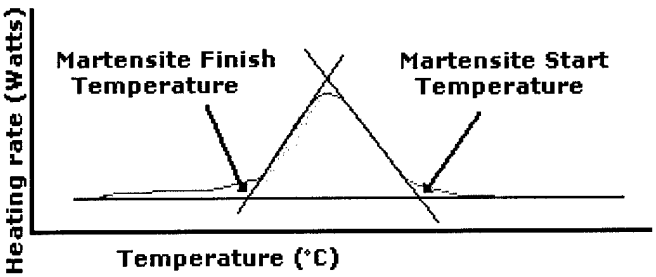

Figure 2: Determination of transition temperatures

Transmission Electron Microscope (TEM) imaging and Diffraction Pattern Analysis were performed by Hans J. Maier and A. Lershe of the University of Paderborn, Germany. TEM images were all taken by a Philips CM 200 TEM operated at a nominal accelerating voltage of 200 kV. To obtain images in the areas around indentations, thin 3 mm disks were removed from a specimen and further thinned using twin-jet electropolishing with a 5% perchloric acid and 95% ethanol solution. This thinning was non-uniform, producing a decreasing thickness in the direction of the center of the disk. After thinning the center to electron transparency, these foils were then indented away from the thinned center region with a Vicker's microindenter at an applied load of 100 mN. The foil was then ion milled to increase the diameter of the electron transparent area until the effects of indentation became visible. Images of these effects were recorded and the electron transparent area was further increased to yield images even closer to the original indentation. TEM images were also taken of the precipitated microstructure for each aging temperature. These samples were produced exclusively by electropolishing.

3. Results

3.1 TEM Imaging

To help characterize the microstructure for each aging treatment, I obtained TEM images of the precipitates to determine precipitate size. Figures 3-7 show these images for the various precipitates. The apparent average size of the precipitates was compared to the scale to determine a rough order of magnitude for the precipitate size. While far from an exact characterization, it is suitable for a general estimate of the precipitate size evolution and provides at better parameter for comparison than the aging temperature, as it provides an objective means of comparison with other experiments given arbitrary heat treatments. Table 1 indicates the apparent precipitate sizes observed.

Aging Temperature	Precipitate Size
623 K	10 nm
673 K	50 nm
723 K	100 nm
773 K	300 nm
823 K	500 nm

Table 1: Apparent precipitate sizes for five aging temperatures

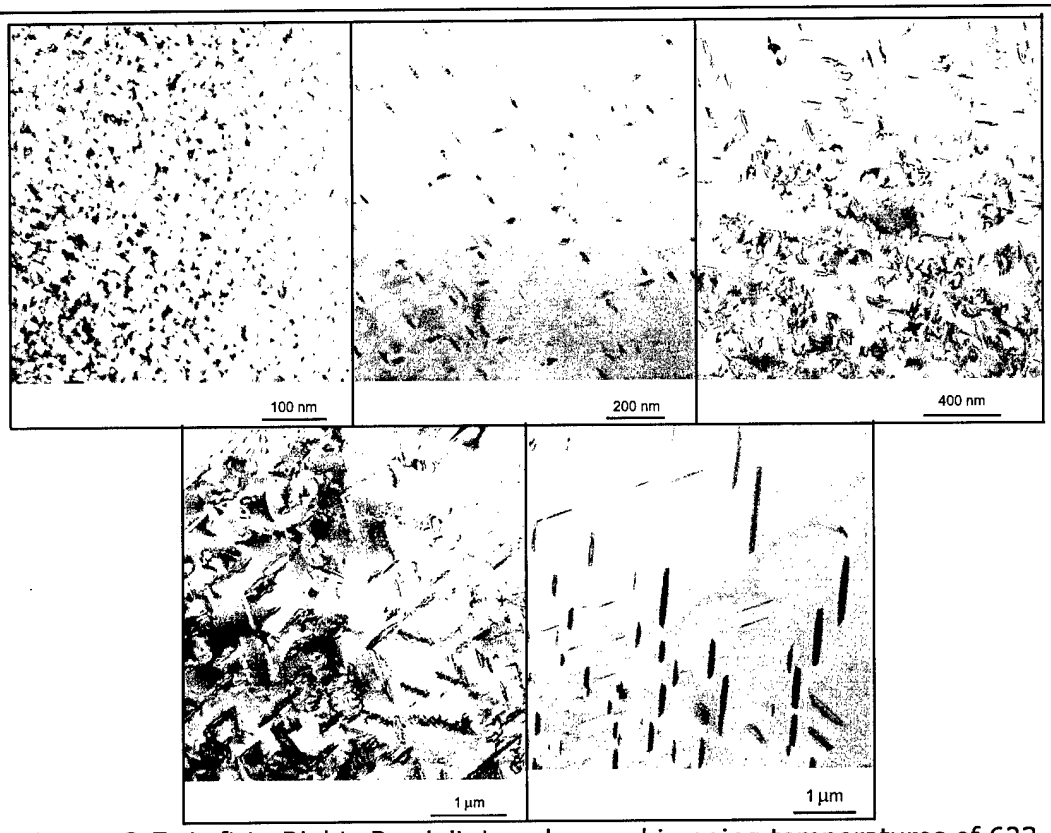

Figures 3-7: Left to Right: Precipitates observed in aging temperatures of 623 K, 673 K, 723 K, 773 K, and 823 K.

TEM imaging was also used to better understand the mechanisms at work when the material was indented. TEM images of the electron-transparent area show the response of the material surrounding micro-indentations. Figures 8-10 show a series of images increasing in magnification of one such area. These images show a certain degree of interaction between the response mechanisms. Martensite plates that are not thermodynamically stable after unloading have had their reverse transformation blocked by concentrations of dislocations. This is fairly conclusive proof that both mechanisms are active during indentation. Their combined presence may cause behavior not expected when considered separately.

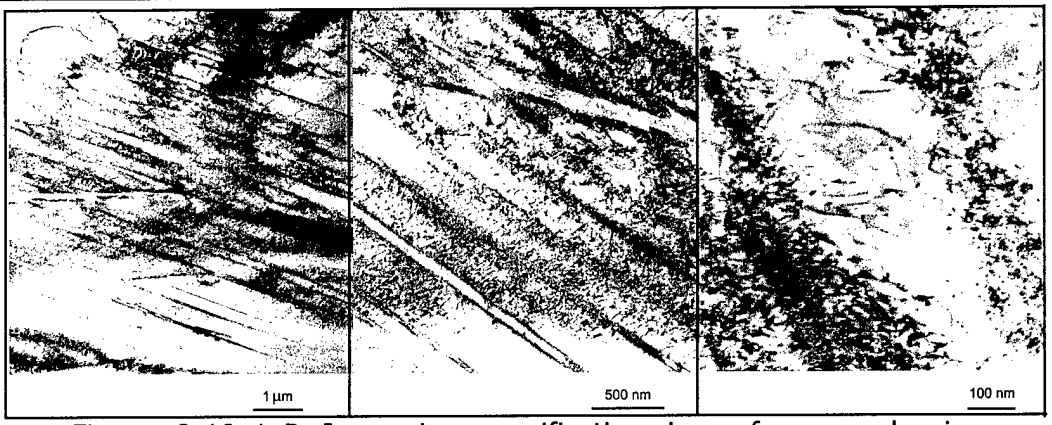

Figures 8-10: L-R: Increasing magnification views of an area showing combined martensite transformation and dislocation activity.

3.2 Diffraction Pattern Analysis

Diffraction pattern analysis was performed on various TEM specimens of aged NiTi to determine the degree of coherence of the particles with the matrix. During aging, precipitates of Ti_3Ni_4 are nucleated from the supersaturated Ni-rich matrix (Seihitoglu et al., 2000). With continued exposure to elevated temperature, these precipitates grow in size. As they grow, the differences in the lattice structures between the precipitate and the parent matrix make maintaining a continuous lattice more difficult. Increasing stress fields develop around the precipitate until lattice discontinuities at the parent-precipitate border are thermodynamically favored. At this point the particle begins to lose coherence with the parent matrix. The diffraction pattern analysis shows large dots (representative of the parent phase) surrounded by smaller dots (representative of the precipitates). The degree to which these dots form around the larger circle in a repeated, symmetrical, and equidistant fashion is a measure of the coherence of the precipitates (Martin, 1998).

These results are purely qualitative, but can be used to show a trend of decreasing coherence with increasing precipitate size within our sample population. Figures 11-13 show the diffraction pattern results for three different aging temperatures. This demonstrates a loss of coherence for particles around 100 nm in size.

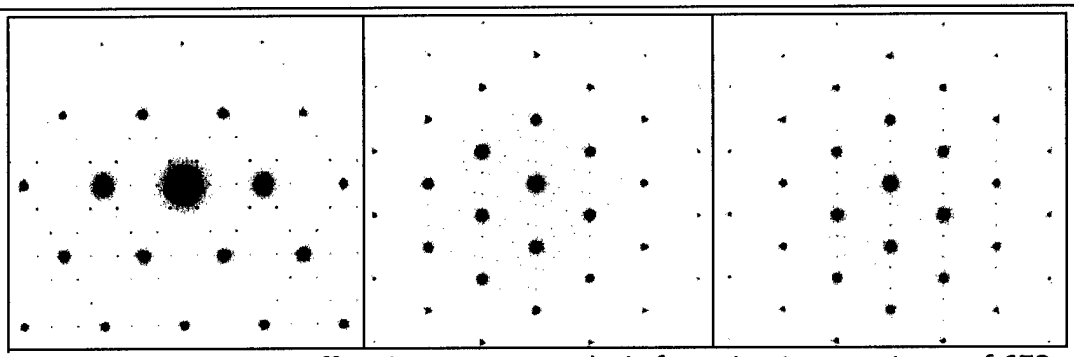

Figures 11-13: L-R: Diffraction pattern analysis for aging temperatures of 673 K, 723 K, and 773 K.

3.3 Differential Scanning Calorimetry

DSC tests were performed for all aging temperatures. The trend shows a mated increase in both austenite and martensite transition temperatures relative to room temperature for small precipitate sizes. After the precipitate particles grow beyond 100 nm, the trend reverses itself. In addition to this reversal, precipitate sizes of 100 nm and higher also experience the intermediate R phase transformation.

An important observation is that, for intermediate precipitate sizes, the test temperature (293 K) falls between the martensite and austenite transformation temperatures. For these specimens, martensite that is transformed during indentation remains stable at room temperature and will not experience a reverse transformation upon unloading (Otsuka and

Wayman, 1998). The trends depicted in Figure 14 below will be used to determine how the resistance to martensitic transformation evolves as precipitate size increases. As the martensite transition temperatures move closer to the test temperature, the applied stress required to induce the transformation decreases, and vice versa.

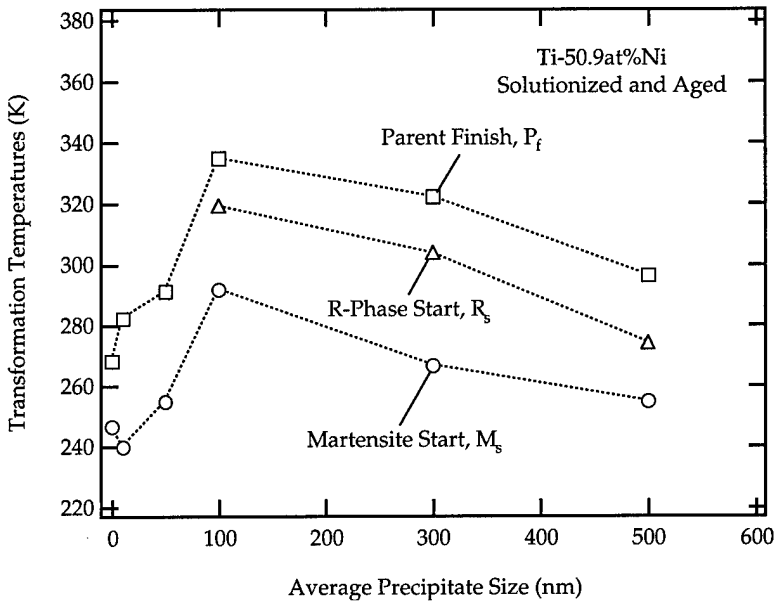

Figure 14: Combined Differential Scanning Calorimetry results.

3.4 Hardness Testing

The combined load vs. depth curves are provided in figures 15-21 respectively for the [100], [110], [111], [210], [221], [221], and [321] orientations. These curves include the loading and unloading behavior during indentation. Each curve is a combined average of ten measurements. The four curves on each graph represent measurements on samples of three distinct heat treatments and a solutionized sample. Hardness values were calculated from the average indentation depth at

maximum load, and are shown in table 2 for all specimens and heat treatments.

	Solutionized	623 K	673 K	723 K	773 K	823 K
[100]	2.18	2.35	2.33	2.01	2.02	2.13
[110]	1.93	2.06	1.79	1.61	1.55	2.04
[111]	2.20	2.39	2.04	2.12	1.92	2.06
[210]	2.23	2.49	2.13	2.11	1.91	1.98
[211]	2.02	2.22	2.01	1.90	1.55	1.91
[221]	1.97	1.97	1.88	1.94	1.84	1.93
[321]	2.02	2.12	1.94	1.63	1.52	2.02

Table 2: Average hardness values (in GPa) for ten indentations.

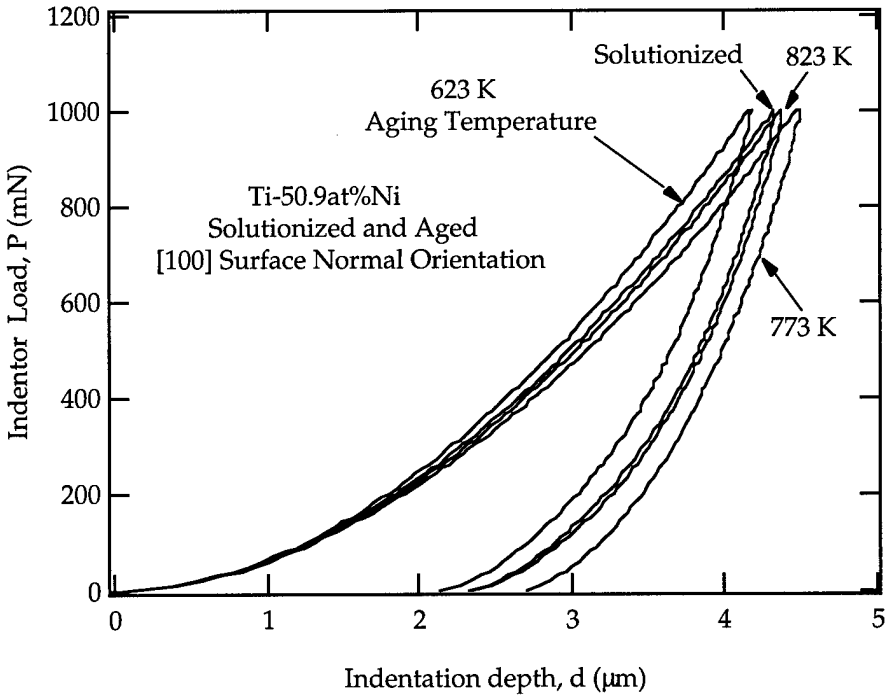

Figure 15: Loading curves for the [100] orientation.

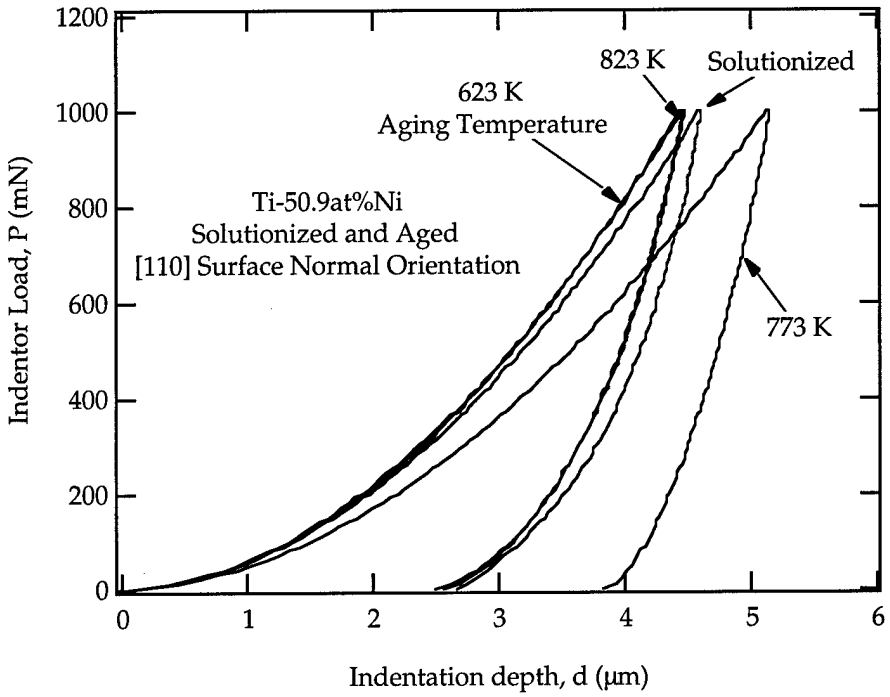

Figure 16: Loading curves for the [110] orientation.

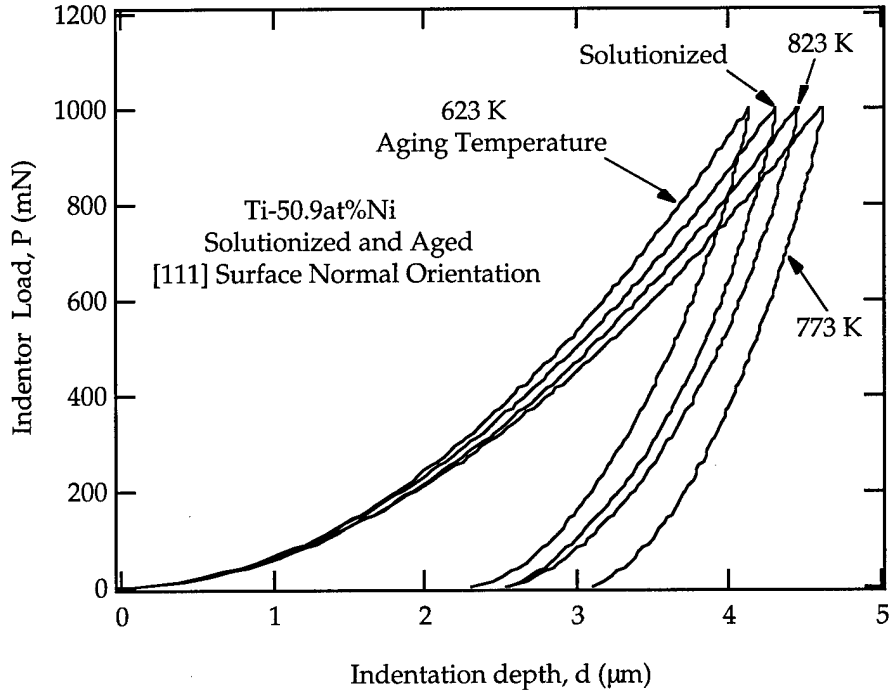

Figure 17: Loading curves for the [111] orientation.

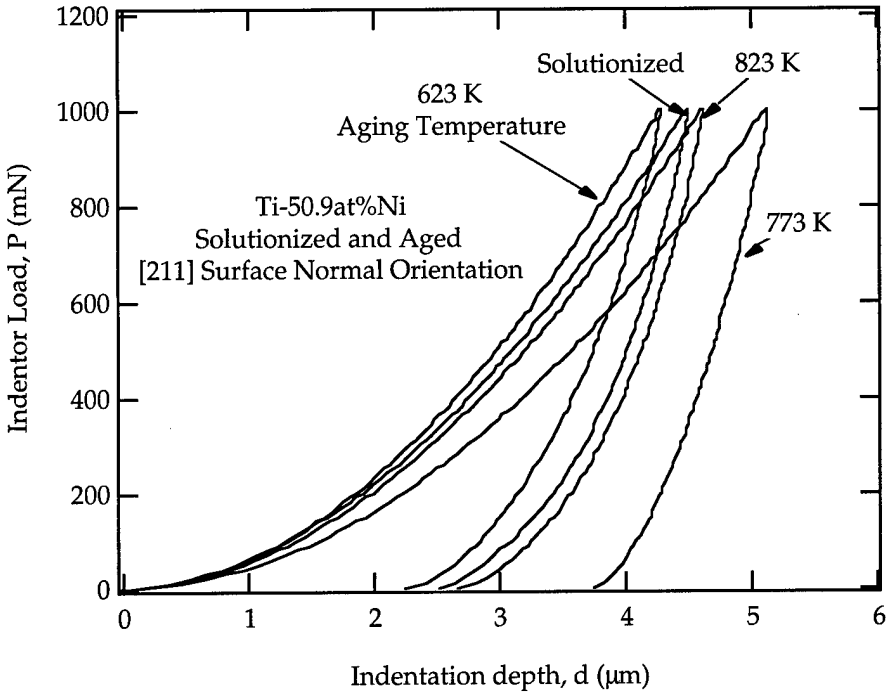

Figure 18: Loading curves for the [211] orientation.

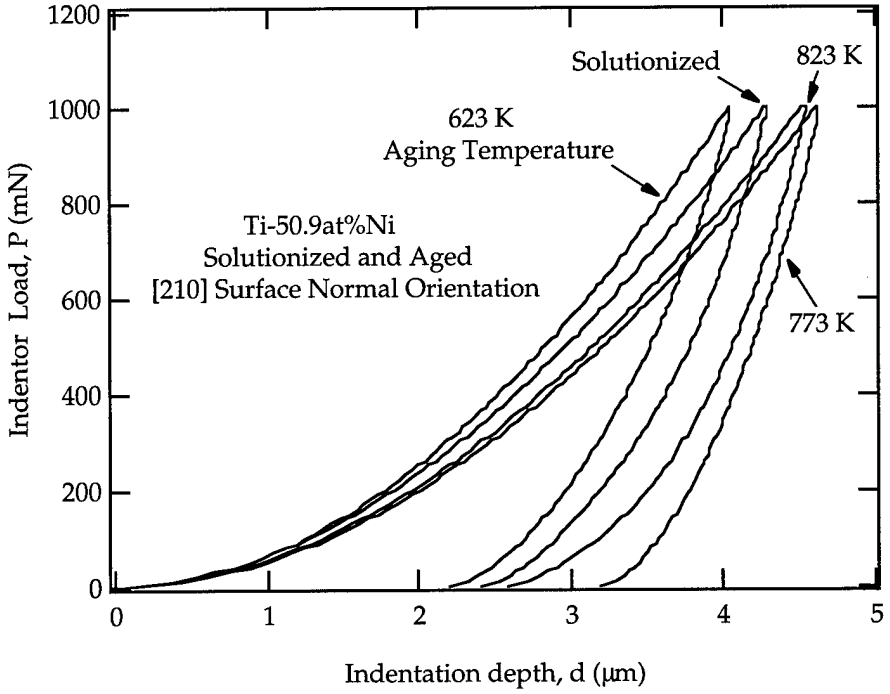

Figure 19: Loading curves for the [210] orientation.

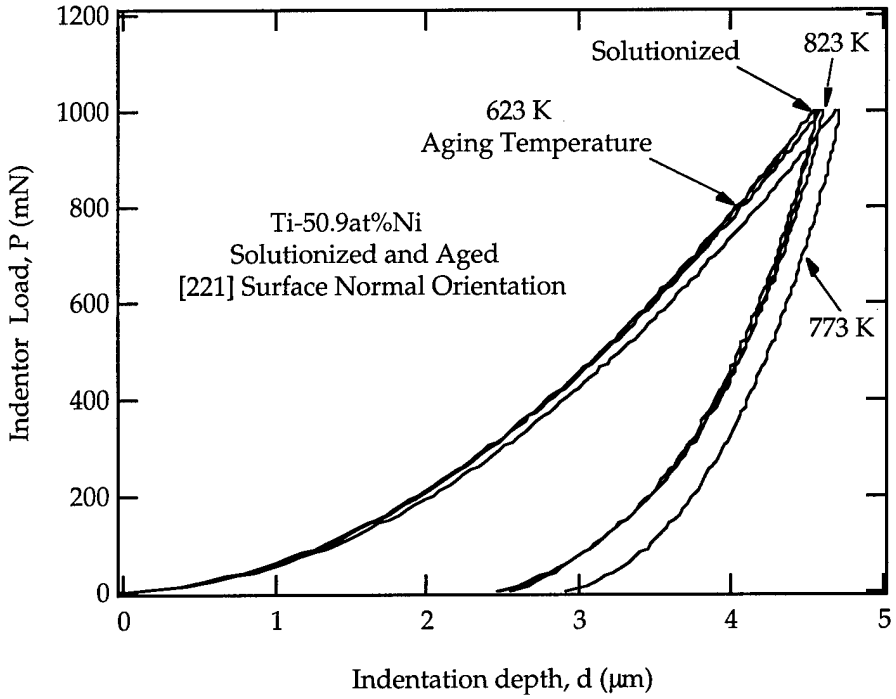

Figure 20: Loading curves for the [221] orientation.

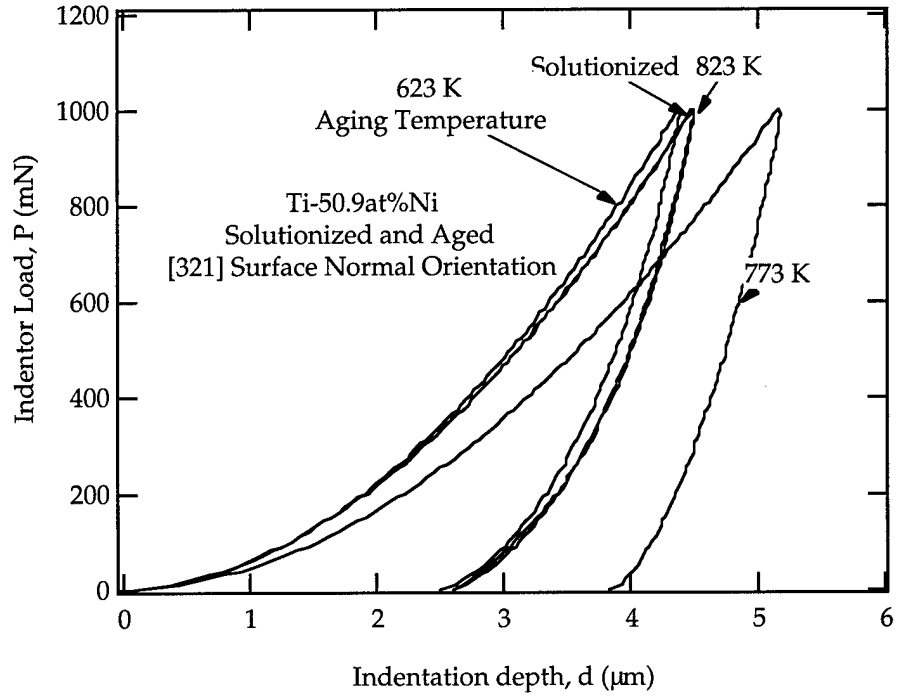

Figure 21: Loading curves for the [321] orientation.

3.5 Elastic Recoverability

The Fischerscope also outputted the measured percentage of energy that was recovered upon unloading. The values for each combination of aging temperature and surface normal orientation are also an average of ten measurements, and are shown in table 3.

	Solutionized	623 K	673 K	723 K	773 K	823 K
[100]	42.13	45.53	44.93	36.95	38.54	42.44
[110]	38.74	39.88	31.48	25.56	25.97	39.70
[111]	40.12	43.14	39.36	31.42	32.83	41.18
[210]	41.87	45.71	34.93	34.02	31.41	38.30
[211]	39.24	44.75	41.60	30.37	28.55	38.23
[221]	39.28	40.37	37.16	30.65	34.69	40.99
[321]	39.52	40.63	31.27	26.68	27.00	39.51

Table 3: Average elastic recoverability (in percent) for ten indentations.

3.6 Cyclic Response to Compression

The stress-strain curves over 100 compressive cycles for each specimen are displayed in figures 22-32. Since changes in the hysteresis loop tended to be more pronounced for the early cycles, the graphs here show stress-strain curves for cycles 1, 2, 4, 8, 16, 32, 64 and 100. This progression is more instructive than a simple cycle interval. Plots were also constructed showing accumulated residual strains over the entire cycle range. This accumulation is sometimes visible in figures 22-33 in

the failure of the hysteresis loop to close upon unloading. In other cases, the residual strains accumulated incrementally over many cycles.

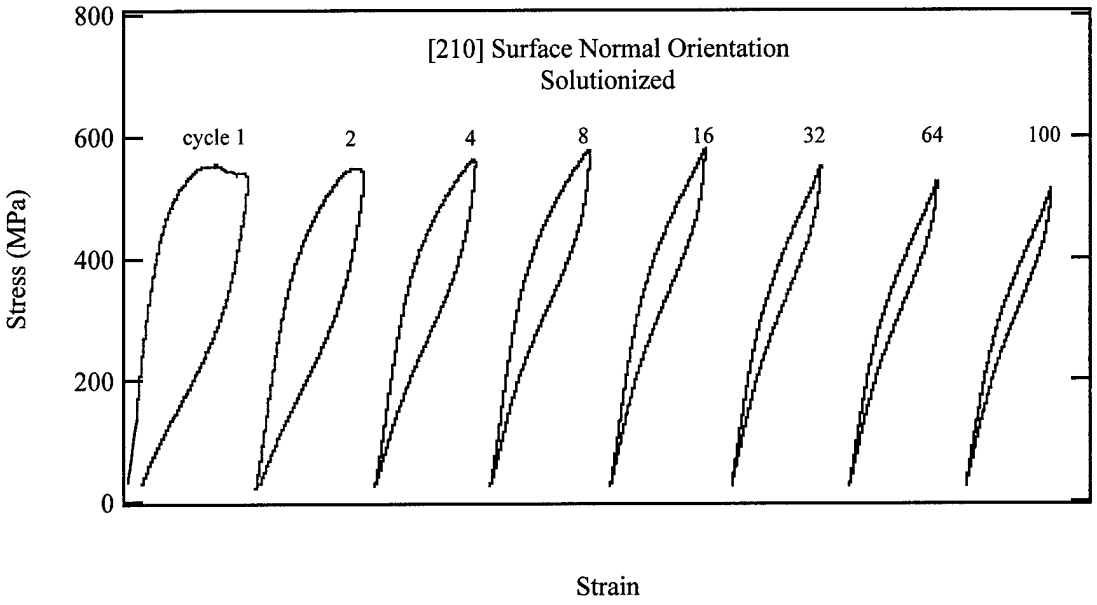

Figure 22: Compressive response of [210] oriented solutionized NiTi

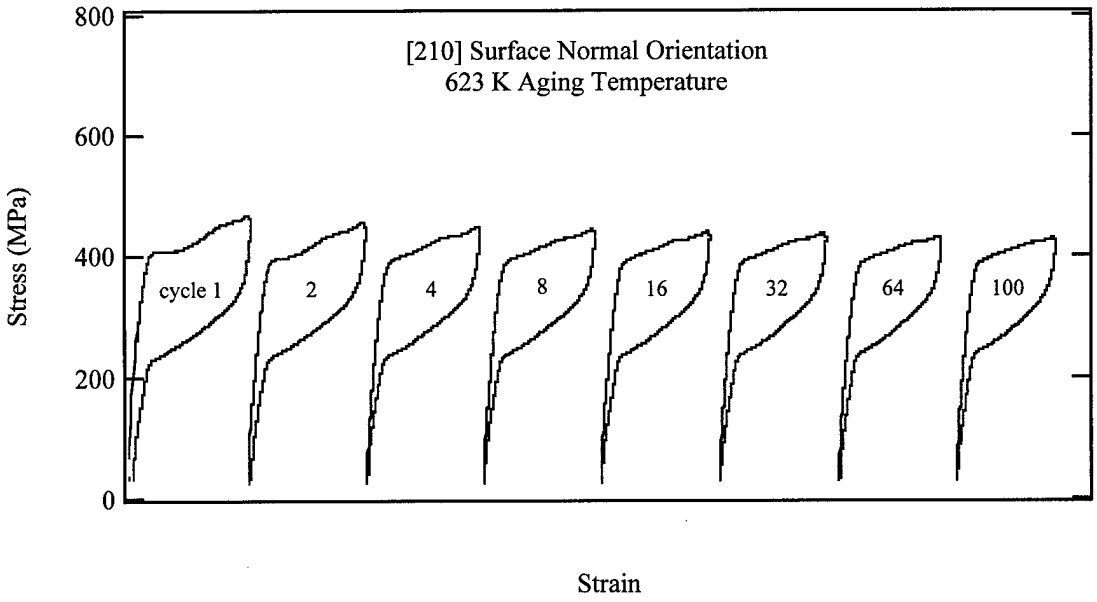

Figure 23: Compressive response of [210] oriented NiTi aged at 623 K

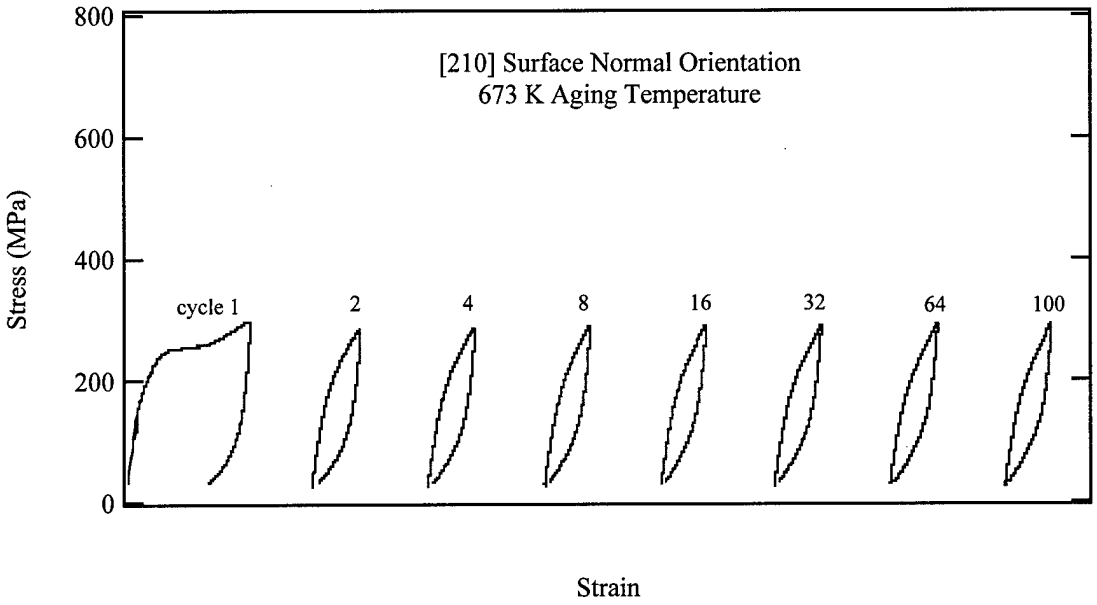

Figure 24: Compressive response of [210] oriented NiTi aged at 673 K

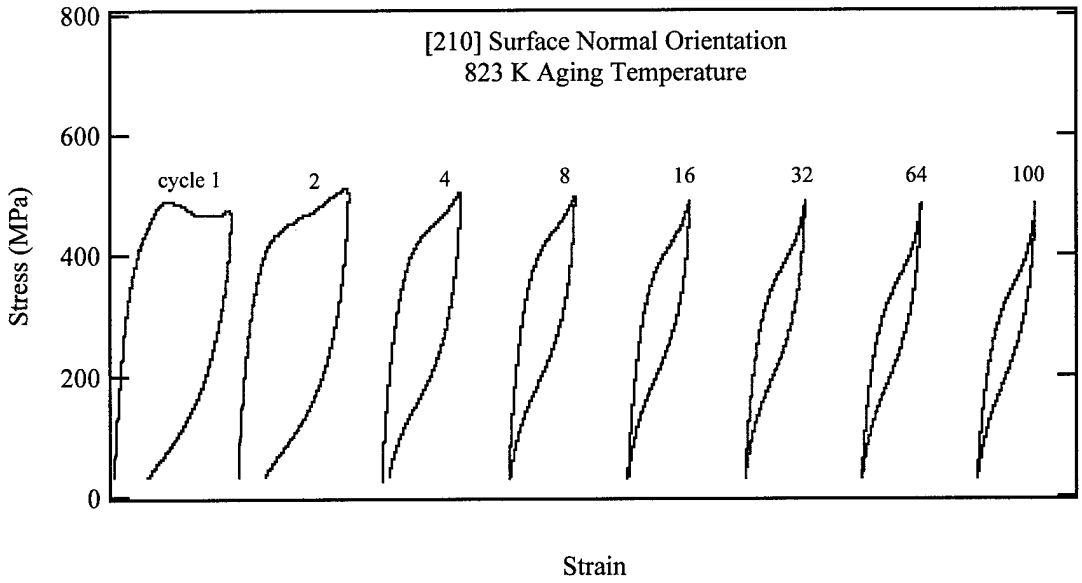

Figure 25: Compressive response of [210] oriented NiTi aged at 823 K

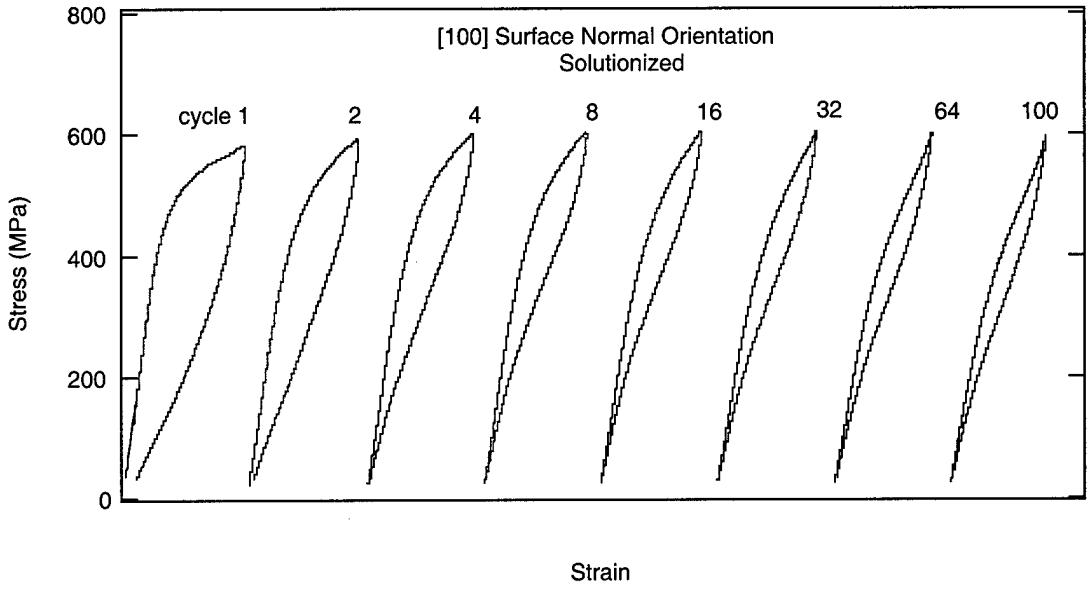

Figure 26: Compressive response of [100] oriented solutionized NiTi

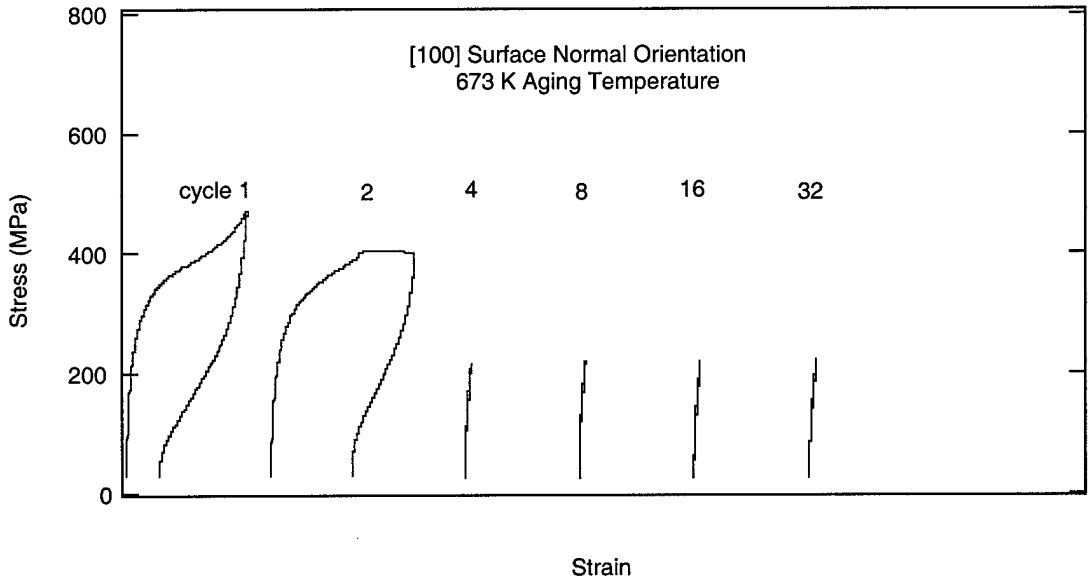

Figure 27: Compressive response of [100] oriented NiTi aged at 673 K

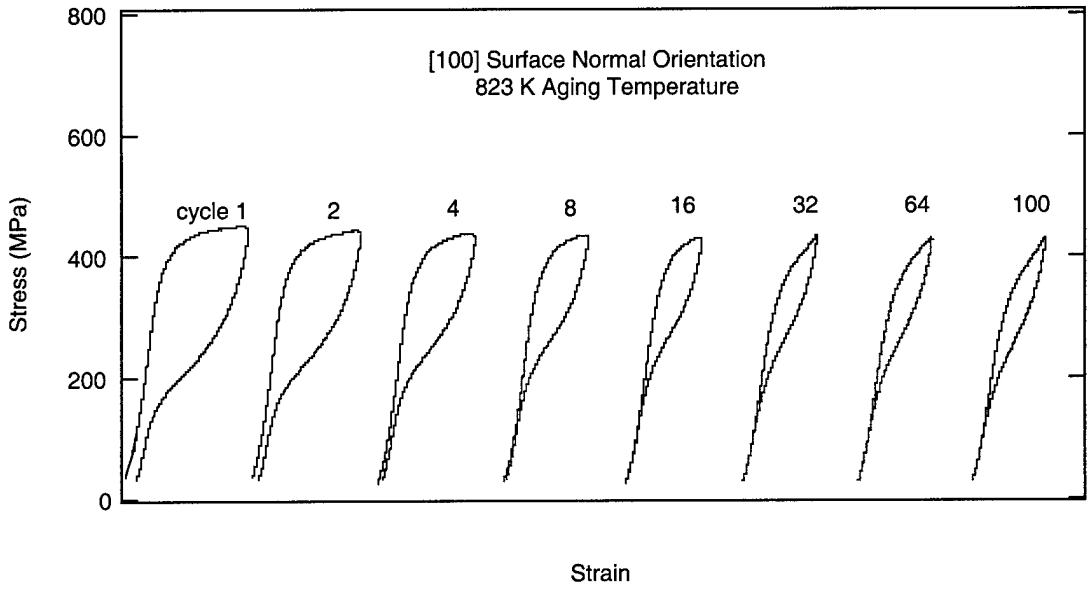

Figure 28: Compressive response of [100] oriented NiTi aged at 823 K

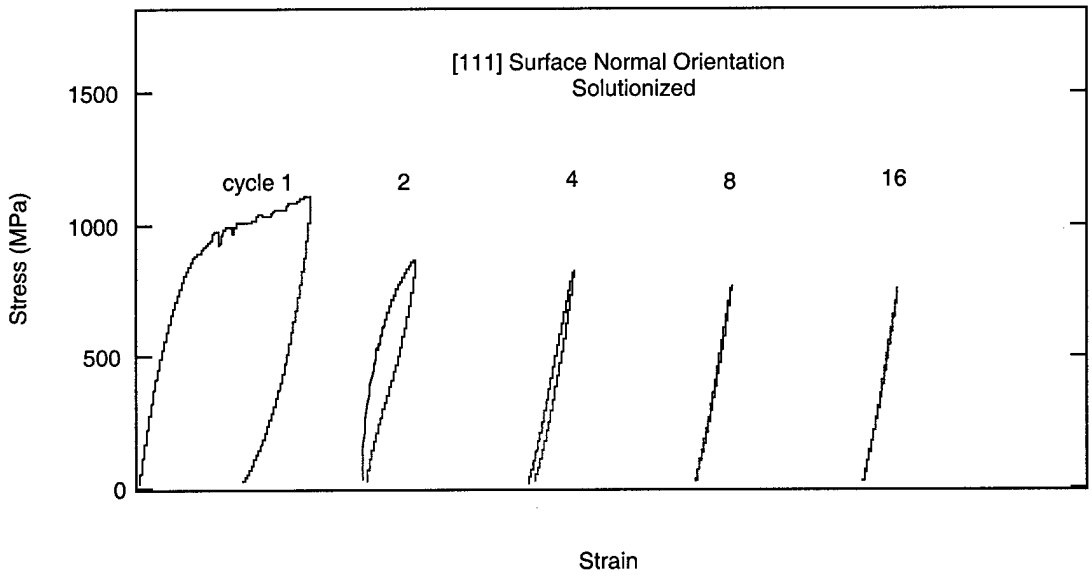

Figure 29: Compressive response of [111] oriented solutionized NiTi

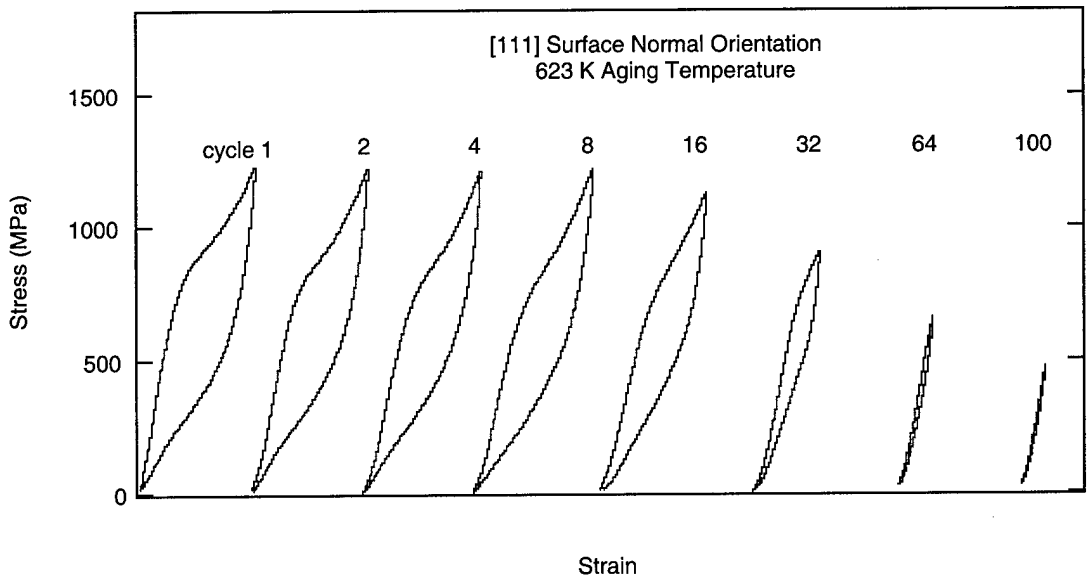

Figure 30: Compressive response of [111] oriented NiTi aged at 623 K

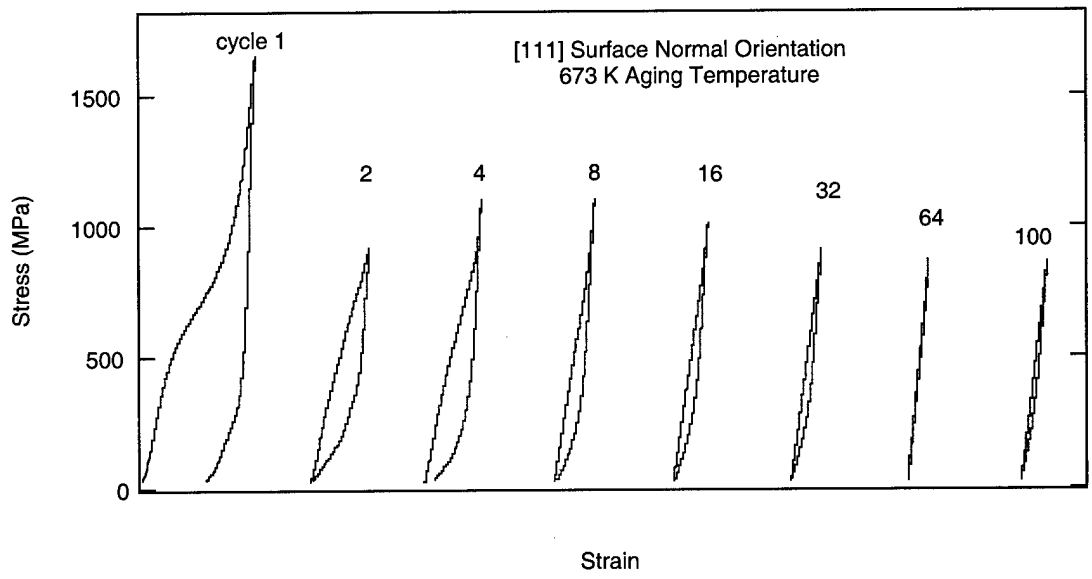

Figure 31: Compressive response of [111] oriented NiTi aged at 673 K

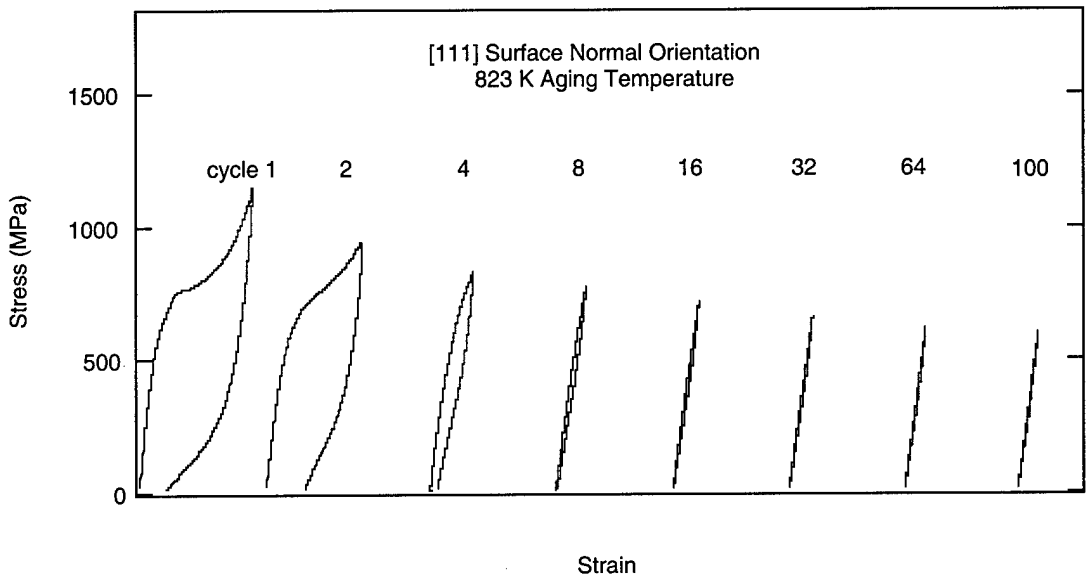

Figure 32: Compressive response of [111] oriented NiTi aged at 823 K

4. Discussion

4.1 Evolution of Hardness with Increasing Precipitate Size

The hardness vs. precipitate size curves for three orientations are presented on figure 33 to show the variation in hardness with changes in precipitate size. Data for all orientations is not shown to preserve the legibility of the graph and only shown major trends. There is an initial increase in hardness at small precipitate sizes. At roughly 25 nm, this increase reaches a peak and begins a rapid decline to the values seen at 100 nm. There is also, however, a slight upturn at the largest precipitate size, and the hardness tends back to that seen at the solutionized state. This behavior is comparable to trends seen in conventional metals, with the exception that they do not decline below solutionized values, or

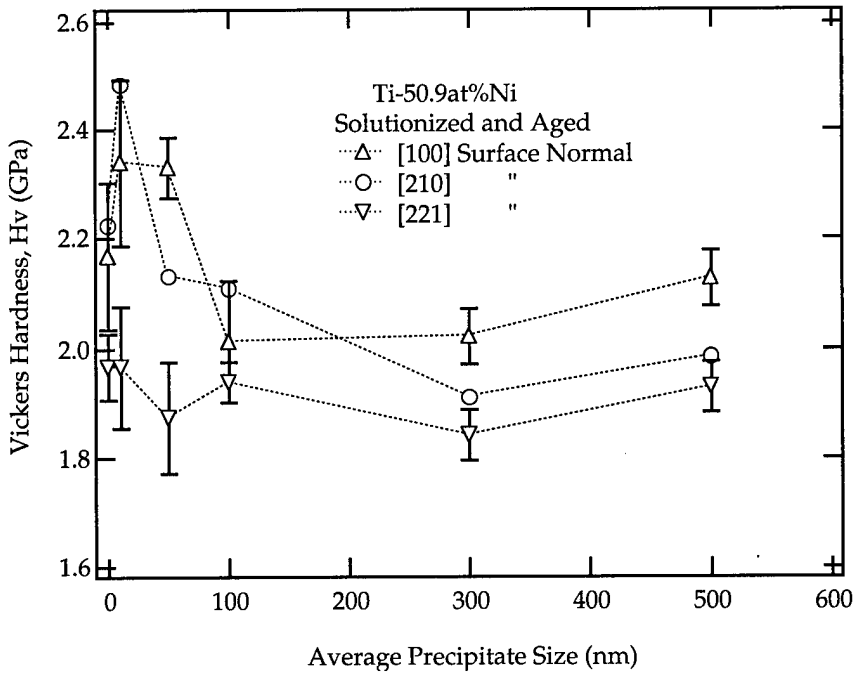

Figure 33: Hardness vs. precipitate size

increase for larger precipitate sizes. The rapid decline at 100 nm precipitate sizes and the decline below solutionized values can both be partially explained by the fact that inducing martensitic transformation is easier at these precipitate sizes due to increasing martensite start temperature.

4.2 Evolution of Elastic Recoverability with Increasing Precipitate Size

The trends for recoverable energy are shown in figure 34. The form of the curve is very similar to that seen for the hardness trends, but slightly more exaggerated. Again there is a steep initial increase for small precipitate sizes, followed by a rapid decline. Here also there is a final

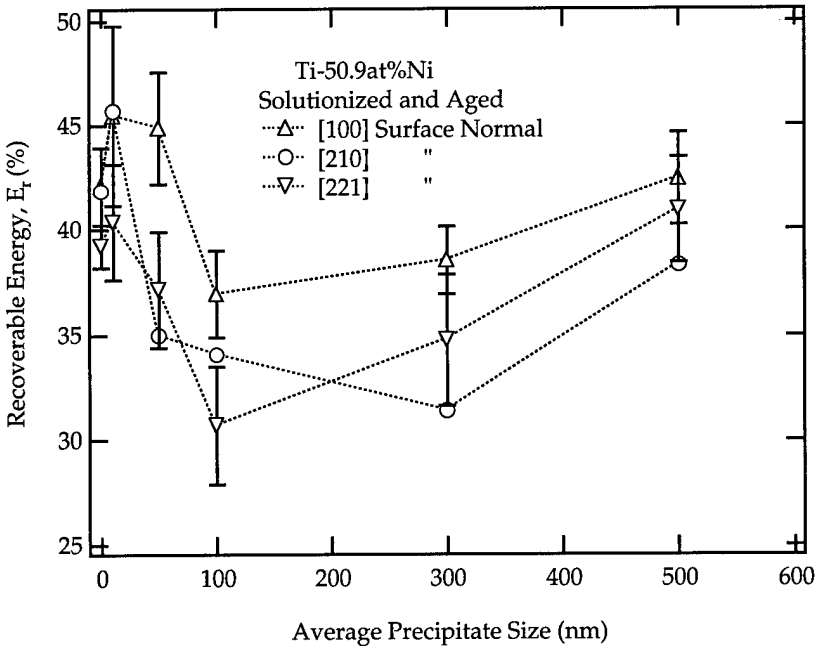

Figure 34: Recoverable energy vs precipitate size

increase at the largest precipitate size. A number of factors determine the amount of recoverability. Lower recoverability could be due to plastic deformation, unstable martensite trapped by dislocation activity, or stabilized martensite due to shape memory effect. Shape memory effect is definitely one of these factors, again seen by the rapid decline at 100 nm precipitate sizes, where martensite becomes stable at room temperature.

4.3 Orientation Effects

For the micro-indentations, the [100] orientation was generally the hardest orientation, and [221] was generally the softest for all heat treatments. This is consistent with experiments performed on similarly oriented solutionized samples (Gall et al., 2000). The orientations sometimes showed a tendency to cross one another, but this is not indicative of a significant trend given the order of variability in the data. Similar trends are seen for elastic recoverability. In general, however, the micro-indentation tests did not strongly indicate a clear orientation effect on the martensitic transformation.

The cyclic compression tests, however, were more telling. For specimens subjected to the same heat treatment, significant variations in the transformation stresses and residual stress accumulations were observed. Figure 35 shows the residual strain accumulation for solutionized specimens of three orientations. The [100] and [210]

specimens are comparable but distinct. The [111] orientation, however, builds up considerably higher residual strains. This is linked to the

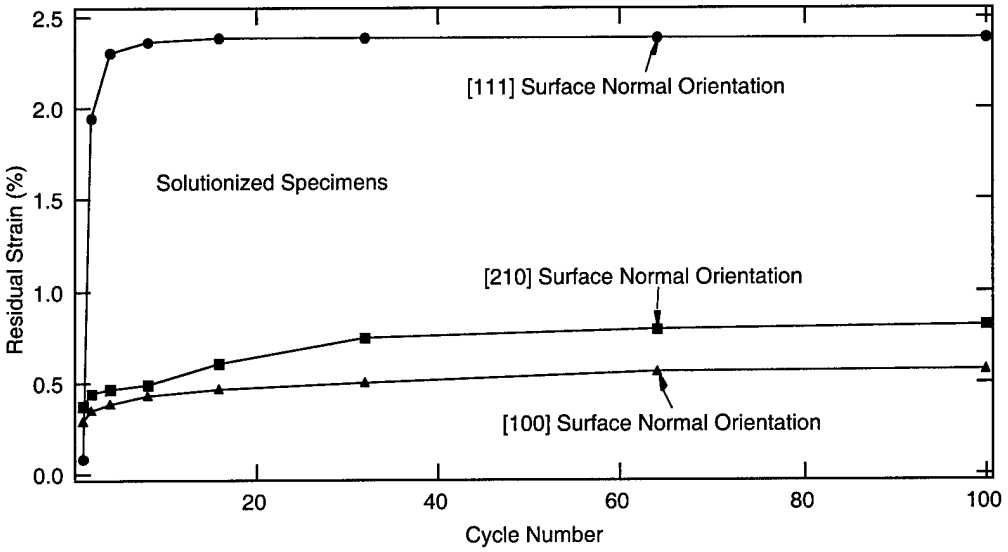

Figure 35: Residual strain accumulation for solutionized [100], [210], and [111] specimens

substantially higher stress levels this orientation must be subjected to in order to achieve -3% strain as well as the favorability of this orientation for slip. As shown in table 4, the stress levels experienced by the [111] specimens are significantly larger than the other two orientations, so higher levels of dislocation activity can be expected, with accompanying residual strain build-up.

	[100]	[210]	[111]
Solutionized	-581 MPa	-540 MPa	-1.11 GPa
623 K	-457 MPa	-466 MPa	-1.23 GPa
673 K	-471 MPa	-291 MPa	-1.65 GPa
823 K	-452 MPa	-483 MPa	-1.15 GPa

Table 4: Maximum stresses experienced in first compressive cycle

From figures 29-32 on pages 33-35, the first cycle stress-strain curves for the [111] orientation indicate that these specimens must experience a larger degree of elastic strain in the martensite phase to reach –3% strain. This difference is attributable to the specific martensite twin variants that are activated during transformation for this orientation in uniaxial loading, which have small associated transformation strains (Sehitoglu et al., 2000). In the complex stress state generated during indentation, the twin variants available will be more diverse and the orientation dependence less defined.

The orientation dependence of associated transformation stresses has been well-documented for similar NiTi single crystal specimens (Gall et al., 2000). Figure 36 shows a stereographic triangle displaying the Schmidt factors associated with transformation stresses among the various orientations.

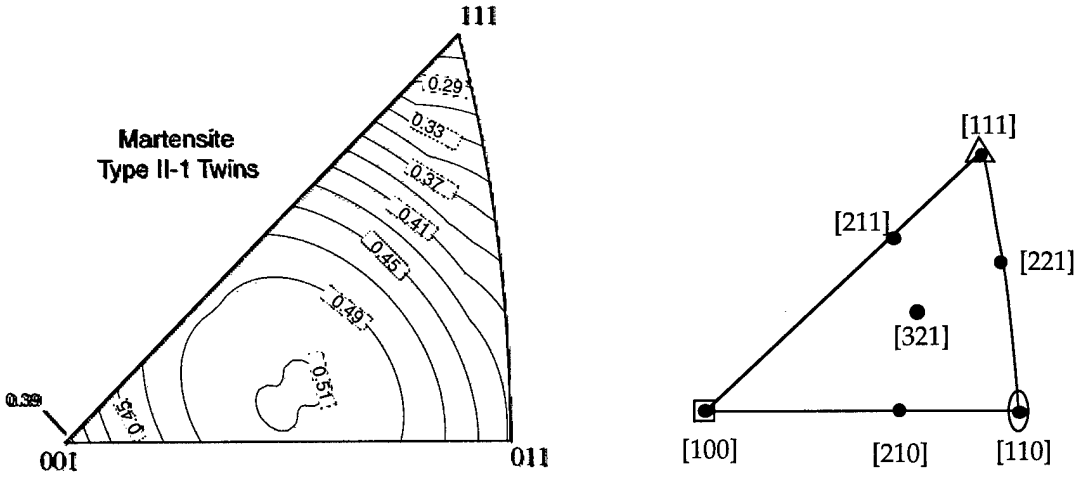

Figure 36: Stereographic triangle depicting Schmidt factors associated with transformation stresses for varying orientations

4.4 Dislocation Activity

Dislocation activity is greatly influenced by the coherence of the precipitates. The introduction of small, highly coherent particles into the matrix for the 623 K aging temperatures causes a sharp increase in the measured hardness. This effect is attributable to the resulting strain fields that surround precipitates with high lattice mismatch parameters. These strain fields increase the energy barrier that must be overcome to advance dislocation movement, so dislocations tend to pile up around the precipitate particles. As the degree of coherency is reduced, the accompanying strain fields lessen and dislocation motion becomes easier. At the point that the particles lose coherency, motion through the matrix resembles that seen in the solutionized state. Measured hardness will not reduce to the solutionized value, however, because the precipitates themselves still provide a barrier to dislocation motion. Since the precipitates are no longer integrated with the matrix, dislocations cannot pass through them. In order to continue moving, the dislocations must either wrap around the precipitates or shear through them (Martin, 1998). Either mechanism requires additional energy.

Surface normal orientation also impacts dislocation motion. The variation in the response of different surface normal orientations to indentation is attributable to the availability of preferred slip systems (Surikova and Chumlyakov, 2000). Previous works (Gall et al., 2000) have documented this dependence, and figure 37 shows stereographic

triangles displaying the associated Schmidt factors for different orientations for the two dominant slip systems.

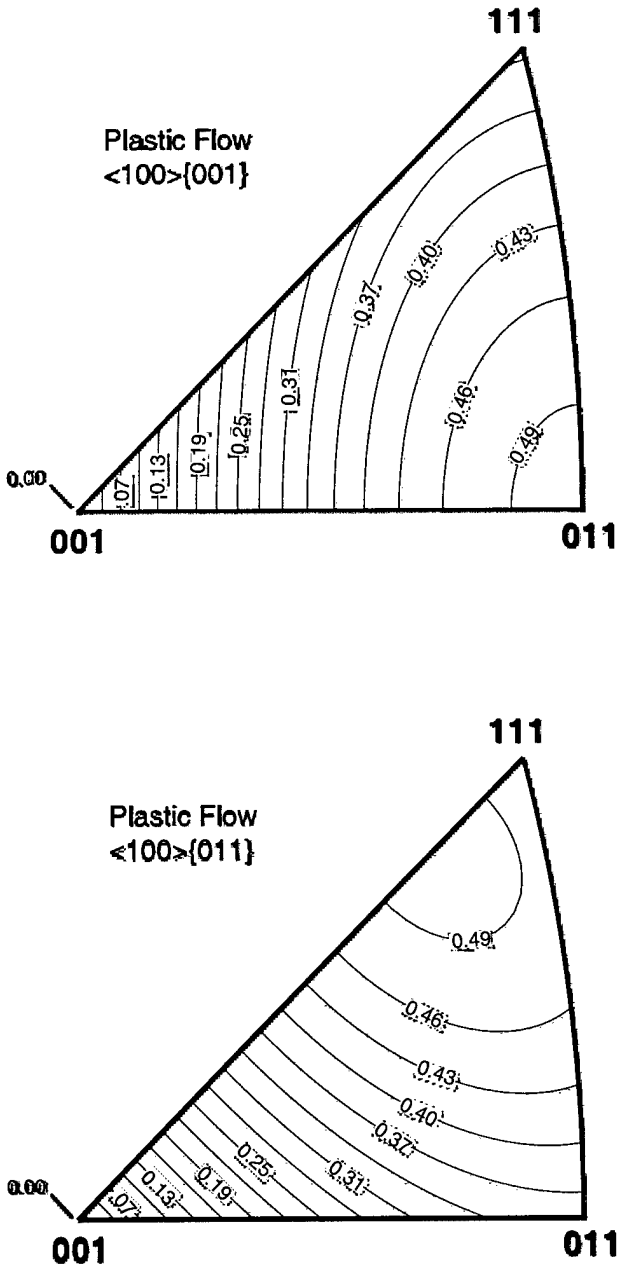

Figure 37: Stereographic triangles depicting Schmidt factors associated with plastic strain for varying orientations

The resistance of the material to plastic flow will dictate how the zone of material around the indentation accommodates energy. Immediately around the indenter tip, we can expect relatively large strains and a high degree of plasticity (Chaudri, 1998). Moving out from this area, greater resistance to dislocation motion will lead to a deformation zone that is deeper and more dominated by elasticity. This will lead to higher observed values of recoverability, as elastic strains are easily reversible upon unloading.

The last impact of dislocation motion is its interaction with the martensitic transformation. Previous TEM images demonstrated that the material does not respond in uniform, progressive stages but through a varied combination. When a region experiences martensitic transformation coupled with dislocation motion, the dislocations can entangle martensite plates and block the reverse transformation. The energy expended to transform such regions of martensite is effectively lost, and the degree of recoverability is reduced.

4.5 Stress-induced Martensitic Transformation

Similar to dislocation activity, a stress-induced martensitic transformation is also greatly influenced by microstructural changes. The strain fields that develop around coherent precipitates work to reduce the stresses required to activate transformation. Since these coherency stresses are additive with applied stresses, the highest strains experienced occur around the precipitates. For this reason, the

martensitic transition is usually initiated there; precipitates will tend to act as nucleation sites for the martensitic transformation. This is reflected in the DSC test results where transformation temperatures rise for small, coherent precipitates. In effect, the ability of the material to resist martensitic transformation is being reduced. At a point around 100 nm precipitate size, this trend reverses itself due to a lowering degree of coherency.

Previous TEM images have demonstrated that martensite that is not thermodynamically stable can have its reverse transformation blocked by dislocations. This has two observed impacts in the cyclic compression tests. First, the reverse transformation becomes incomplete and residual strains accumulate. Second, successive martensitic transformations can be more easily initiated if there are already sections of martensite in the specimen.

Due to the increasing presence of trapped martensite, the transformation behavior of NiTi can change quickly over the course of several compressive cycles. The first cycle generally has a well-defined stress-strain curve with three distinct regions for elastic deformation of austenite, martensitic transformation, and elastic deformation of martensite. Succeeding cycles erode the sharp definition of these regions. Martensite trapped by dislocation activity will facilitate localized transformation at lower stress levels for future transformations. As these regions of trapped martensite grow in number and residual strains accumulate, the mechanisms that shape the stress-strain response begin

to occur simultaneously. Instead of the sharply defined regions dominated by distinct mechanisms, the stress-strain curve becomes a non-linear response influenced by competing factors. Figure 32 on page 35 provides the clearest exhibition of this behavior.

Repeated martensitic transformation is thereby sensitive to the effects of dislocation activity. For orientations that are not favorably oriented to activate slip systems, dislocation activity is lower and less degradation of the transformation is expected over repeated cycles.

4.6 Evolution of Cyclic Compressive Response with Increasing Precipitate Size

The effect of precipitate coherency and size on the martensitic transformation is directly observable from the differences in the stress levels in the cyclic compression tests for different heat treatments of the same orientation. In figure 22 on page 30, stresses of approximately 550 MPa are required to induce transformation for cycle 1 in the solutionized [210] specimen. For the 623 K heat treatment in figure 23, this initial transformation stress drops to 400 MPa. The 673 K heat-treated specimen on figure 24 has transformation temperatures very close to the test temperature, accompanied by very small initial transformation stresses of 250 MPa. It is evident from the large residual strain accumulated on the first cycle that the reverse transformation was still

underway at the point unloading stopped. For the 823 K heat treatment in figure 25, precipitate coherency has dropped significantly, and the transformation begins at a much higher stress level of roughly 500 MPa. This trend of fluctuating initial transformation stresses is paralleled by the changes in transition temperatures from the DSC tests.

The mild heat treatments, shown by indentation to reduce dislocation activity through higher measured hardness, should also improve the repeatability of the transformation. This is demonstrated in figure 38, which plots the accumulated strain for the [210] orientation for the solutionized specimen and the 623 K and 823 K heat treatments. The 623 K heat treatment, with its small, coherent precipitates, reduces dislocation activity while facilitating transformation. It consistently develops lower residual strains over 100 cycles. This logic would also infer that the 823 K heat treatment residual strains should be still lower than but approaching the solutionized values. However, the transition

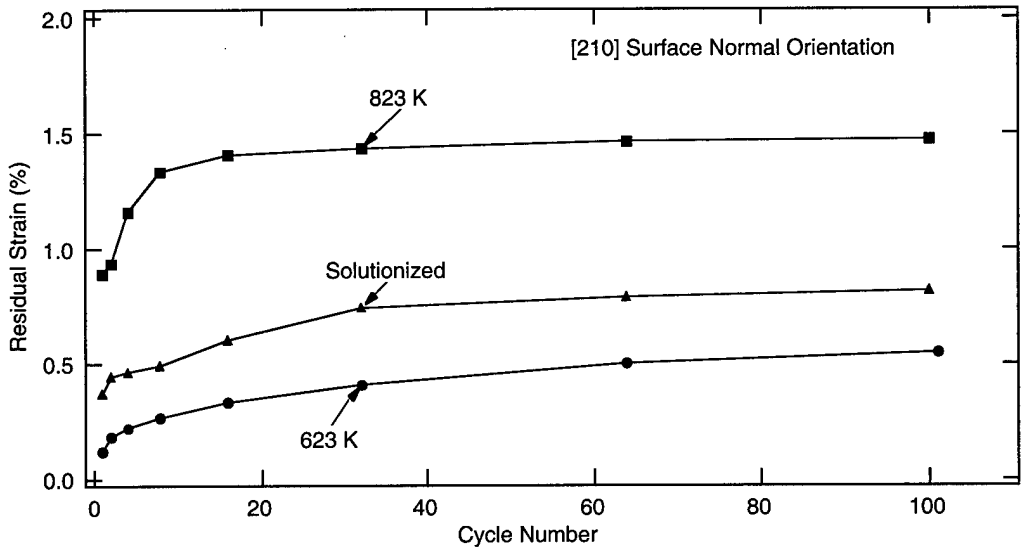

Figure 38: Residual strain accumulation for the [210] orientation

temperatures for this heat treatment are close to the test temperature, and the residual strains shown here may include an incomplete transformation due to an insufficient driving force for the reverse transformation.

Qualitative validation of this behavior can be observed in changes in the size and shape of the hysteresis loop over 100 cycles. Referring back to figures 22-25 on pages 30 and 31, the solutionized and 823 K heat-treated [210] specimens gradually lose definition over the cycle range and revert towards thin bands resembling an elastic response. The 623 K heat treatment, however, retains its basic shape over the entire range. While residual strains are accumulating, the effect is much less pronounced for this heat treatment.

4.7 Statistical Analysis

A thorough examination of the data would be incomplete without a look at the statistical significance of the data. A simple comparison of means is not instructive in this case. A more informative study would involve an analysis of the variance to determine the significant sources of variation. Tables 5 and 6 at the end of this section provide respective two factor analyses of variance with replication for the measured hardness and elastic recoverability at a 95% significance level. The results for both measurements are similar. Aging temperature proves to be the largest source of variation. Orientation, while still significant, is less of a factor.

Interaction effects are present but of little consequence compared to the first two factors. This is to be expected, as previous studies have indicated that peak aged NiTi exhibits less orientation dependence than solutionized or over-aged specimens (Chumlyakov and Starenchenko, 1995). Random variations are not significant. Based on this analysis, aging temperature and orientation are assumed to be the primary influences on the response.

Table 5: Two-factor Analysis of Variance with Replication for Measured Hardness

SUMMARY *[100]*	Sol't	350.00	400.00	450.00	500.00	550.00	Total
Count	10.00	10.00	10.00	10.00	10.00	10.00	60.00
Sum	21.79	23.46	23.27	20.15	20.25	21.29	130.20
Average	2.18	2.35	2.33	2.01	2.02	2.13	2.17
Variance	0.02	0.02	0.00	0.01	0.00	0.00	0.03
[110]							
Count	10.00	10.00	10.00	10.00	10.00	10.00	60.00
Sum	19.27	20.57	17.94	16.13	15.47	20.42	109.79
Average	1.93	2.06	1.79	1.61	1.55	2.04	1.83
Variance	0.00	0.00	0.01	0.00	0.00	0.00	0.04
[111]							
Count	10.00	10.00	10.00	10.00	10.00	10.00	60.00
Sum	21.96	23.88	20.36	21.15	19.19	20.61	127.15
Average	2.20	2.39	2.04	2.12	1.92	2.06	2.12
Variance	0.00	0.02	0.00	0.01	0.00	0.02	0.03
[210]							
Count	10.00	10.00	10.00	10.00	10.00	10.00	60.00
Sum	22.26	24.86	21.35	21.12	19.10	19.85	128.55
Average	2.23	2.49	2.13	2.11	1.91	1.98	2.14
Variance	0.00	0.01	0.01	0.01	0.00	0.00	0.04
[211]							
Count	10.00	10.00	10.00	10.00	10.00	10.00	60.00
Sum	20.20	22.19	20.08	19.03	15.52	19.14	116.14
Average	2.02	2.22	2.01	1.90	1.55	1.91	1.94
Variance	0.00	0.00	0.00	0.01	0.00	0.00	0.04
[221]							
Count	10.00	10.00	10.00	10.00	10.00	10.00	60.00
Sum	19.65	19.72	18.79	19.39	18.43	19.32	115.29
Average	1.97	1.97	1.88	1.94	1.84	1.93	1.92
Variance	0.00	0.01	0.01	0.00	0.00	0.00	0.01
[321]							
Count	10.00	10.00	10.00	10.00	10.00	10.00	60.00
Sum	20.18	21.24	19.43	16.26	15.25	20.20	112.55
Average	2.02	2.12	1.94	1.63	1.52	2.02	1.88
Variance	0.01	0.02	0.01	0.00	0.00	0.00	0.05
Total							
Count	70.00	70.00	70.00	70.00	70.00	70.00	
Sum	145.31	155.91	141.21	133.23	123.20	140.83	
Average	2.08	2.23	2.02	1.90	1.76	2.01	
Variance	0.02	0.04	0.03	0.04	0.04	0.01	

ANOVA

Source of Variation	*SS*	*df*	*MS*	*F*	*P-value*	*F crit*
Orientation	7.08	6.00	1.18	198.93	0.00	2.12
Aging Temperature	8.74	5.00	1.75	294.49	0.00	2.24
Interaction Effects	3.44	30.00	0.11	19.30	0.00	1.49
Random Effects	2.24	378.00	0.01			
Total	21.50	419.00				

Table 6: Two-factor Analysis of Variance with Replication for Elastic Recoverability

SUMMARY *[100]*	Sol't	350.00	400.00	450.00	500.00	550.00	Total
Count	10.00	10.00	10.00	10.00	10.00	10.00	60.00
Sum	421.29	455.29	449.25	369.51	385.39	424.35	2505.08
Average	42.13	45.53	44.93	36.95	38.54	42.44	41.75
Variance	3.52	18.76	7.03	4.53	2.75	5.04	16.23
[110]							
Count	10.00	10.00	10.00	10.00	10.00	10.00	60.00
Sum	387.35	398.76	314.82	255.58	259.65	397.00	2013.16
Average	38.74	39.88	31.48	25.56	25.97	39.70	33.55
Variance	0.25	1.07	9.99	0.29	2.33	3.18	41.66
[111]							
Count	10.00	10.00	10.00	10.00	10.00	10.00	60.00
Sum	401.16	431.36	393.56	314.15	328.31	411.76	2280.30
Average	40.12	43.14	39.36	31.42	32.83	41.18	38.01
Variance	0.14	0.88	9.79	2.40	2.21	17.03	24.08
[210]							
Count	10.00	10.00	10.00	10.00	10.00	10.00	60.00
Sum	418.65	457.14	349.26	340.15	314.12	382.95	2262.27
Average	41.87	45.71	34.93	34.02	31.41	38.30	37.70
Variance	0.24	0.53	5.73	2.34	0.51	0.77	25.74
[211]							
Count	10.00	10.00	10.00	10.00	10.00	10.00	60.00
Sum	392.41	447.49	415.97	303.65	285.49	382.33	2227.34
Average	39.24	44.75	41.60	30.37	28.55	38.23	37.12
Variance	1.05	2.42	1.72	2.34	1.81	0.26	35.89
[221]							
Count	10.00	10.00	10.00	10.00	10.00	10.00	60.00
Sum	392.76	403.74	371.62	306.48	346.92	409.92	2231.44
Average	39.28	40.37	37.16	30.65	34.69	40.99	37.19
Variance	1.11	7.82	7.80	8.02	9.90	6.54	19.50
[321]							
Count	10.00	10.00	10.00	10.00	10.00	10.00	60.00
Sum	395.21	406.32	312.69	266.77	269.98	395.13	2046.10
Average	39.52	40.63	31.27	26.68	27.00	39.51	34.10
Variance	1.27	3.50	4.18	0.32	0.54	0.66	38.02
Total							
Count	70.00	70.00	70.00	70.00	70.00	70.00	
Sum	2808.83	3000.10	2607.17	2156.29	2189.86	2803.44	
Average	40.13	42.86	37.25	30.80	31.28	40.05	
Variance	2.56	10.21	28.74	16.15	20.12	6.49	

ANOVA

Source of Variation	*SS*	*df*	*MS*	*F*	*P-value*	*F crit*
Orientation	2663.47	6.00	443.91	114.67	0.00	2.12
Aging Temperature	8714.66	5.00	1742.93	450.23	0.00	2.24
Interaction Effects	1688.22	30.00	56.27	14.54	0.00	1.49
Random Effects	1463.32	378.00	3.87			
Total	14529.67	419.00				

5. Conclusions

Effects of precipitate size:

- For the smallest particle size of 10 nm, the degree of coherence is highest and the martensite transition temperature is furthest from the reference room temperature. This size maximizes hardness and elastic recoverability, and reduces irreversibilites in the martensitic transformation.
- As particle size increases from 50 nm to 100 nm, the degree of coherence declines and the martensitic transformation temperature increases. Measured values of hardness and elastic recoverability drop and irreversibilities in the martensitic transformation increase.
- For precipitates between 100 nm and 500 nm, the coherence of the particles continues to diminish and the resistance to plastic deformation is approaching that of the solutionized state. The martensitic transformation, however, is becoming more difficult as the transition temperature decreases.

These trends are highlighted on figure 39, which shows the combined hardness and elastic recoverability as an average for all orientations.

Effects of orientation:

- For the complex stress state seen in indentation, orientation dependence is very low compared to the macroscale response.

- In uniaxial loading, the orientation affects both dislocation motion and the transformation stresses. [100] is found to strongly resist dislocation motion, while the [111] and [110] orientations facilitate it. [111] is found to strongly resist martensitic transformation, while [210] greatly facilitates it.
- Orientations that either resist the martensitic transformation or facilitate dislocation motion tend to accumulate large residual strain and demonstrate poor repeatability in their cyclic compression response.

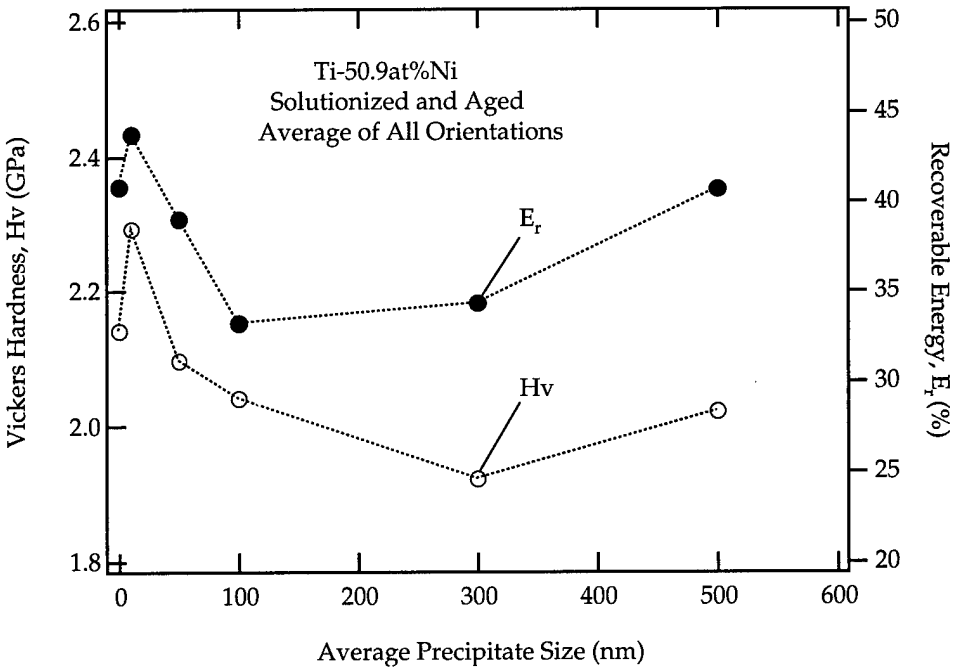

Figure 39: Combined hardness and elastic recoverability for all orientations.

6. References

Brailovski V. and Trochu F.; "A Review of Shape Memory Alloys Medical Applications"; *BIO-MEDICAL MATERIALS AND ENGINEERING;* 1996; vol. 6; pp. 291-298.

Chaudhri M. M.; "Subsurface Strain Distribution around Vicker's Hardness Indentations in Annealed Polycrystalline Copper"; *ACTA MATERIALIA*; 1998; vol. 46;pp. 3047-3056.

Chumlyakov Y. I., and Starenchenko S. V.; "Stress-induced Martensitic Transformation in Aged Titanium Nickel Single Crystals"; *JOURNAL DE PHYSIQUE IV*; 1995; vol. 5; pp. 803-807.

Doerner M. F. and Nix W. D.; "A Method for Interpreting the Data from Depth-Sensing Indentation Instruments"; *JOURNAL OF MATERIALS RES.*; 1986; vol. 1; pp. 601-609.

Elban W. L. and Armstrong R. W.; "Plastic Anisotropy and Cracking at Hardness Impressions in Single Crystal Ammonium Perchlorate"; *ACTA MATERIALIA;* 1998; vol. 46; pp. 6041-6052.

Gall K., Dunn M. L., Liu Y., Labossiere P., Sehitoglu H., and Chumlyakov Y.; "Micro and macro deformation of oriented NiTi single crystals"; *JOURNAL OF ENGINEERING MATERIALS AND TECHNOLOGY*; 2000; In review.

Gall K., Sehitoglu H., Chumlyakov Y. I., and Kireeva I.; "Pseudoelastic Cyclic Stress-strain Response of Overaged Single Crystal Ti-50.8%Ni"; *SCRIPTA MATERIALIA*; 1999; vol. 40; pp. 7-12.

Gall K., Sehitoglu H., Chumlyakov Y. I., Kireeva I., and Maier H. J.; "The Influence on Critical Transformation Stress Levels and Martensite Start Temperatures in NiTi: Part I Discussion of Experimental Results"; *JOURNAL OF ENGINEERING MATERIALS AND TECHNOLOGY*; 1999; vol. 121; pp. 19–27.

Gall K., Sehitoglu H., Chumlyakov Y. I., Kireeva I., and Maier H. J.; "The Influence of Aging on Critical Transformation Stress Levels and Martensite Start Temperatures in NiTi: Part II Aged Microstructure and Modeling"; *JOURNAL OF ENGINEERING MATERIALS AND TECHNOLOGY*; 1999; vol. 121; pp. 28-37.

Giannakopoulos A.E., Larsson P.L., and Vestergaard R.; "Analysis of Vickers indentation"; *INTERNATIONAL JOURNAL OF SOLIDS AND STRUCTURES*; Vol. 31: (19) 2679-2708; 1994.

Giannakopoulos A.E. and Suresh S.; "Determination of elastoplastic properties by instrumented sharp indentation"; *SCRIPTA MATERIALIA*; 1999; Vol. 40: (10) 1191-1198.

Gil F.X., Manero J.M., and Planell J.A.; "Relevant aspects in the clinical applications of NiTi shape memory alloys"; *JOURNAL OF MATERIALS SCIENCE*; 1996; Vol. 7: 403-406.

Hay J. L. and Pharr G. M.; *ASM HANDBOOK, MECHANICAL TESTING;* Vol. 8; pp. 231-242.

Ishida A. and Miyazaki S.; "Microstructure and Mechanical Properties of Sputter-Desposited Ti-Ni Alloy Thin Films"; *JOURNAL OF ENGINEERING MATERIALS AND TECHNOLOGY*; 1999; vol. 121; pp. 2-8.

Johnson A. D.; *MICROMACHINE DEVICES*; 1999; vol. 4; pp. 1.

Krulevitch P., Lee A. P., Ramsey P. B., Trevino J., and Northrup M. A.; "Thin Film Shape Memory Alloy Microactuators"; *JOURNAL OF MICROELECTROMECHANICAL SYSTEMS (MEMS)*; 1996; vol. 59; pp. 301-306.

Liu R., Li D.Y., Xie Y.S., Llewellyn R., and Hawthorne H.M; "Indentation behavior of psuedoelastic TiNi alloy"; *SCRIPTA MATERIALIA*; 1999; Vol. 41: (7) 691-696.

Liu Y., Xie Z., Humbeeck J. V., Delaey L. AND Lui Y.N.; "On the Deformation of the Twinned Domain in NiTi Shape Memory Alloys"; *PHILOSOPHICAL MAGAZINE A*; 2000; vol. 80; pp. 1935-1953.

Martin J. W.; "Precipitation Hardening"; Second Edition; Butterworth-Heinemann Press, Woburn, MA; 1998; pp 9-11

Oliver W. C. and Pharr G. M.; "An Improved Technique for Determining Hardness and Elastic Modulus Using Load and Displacement Sensing Indentation Experiments,"; *JOURNAL OF MATERIALS RES.*; 1992; vol. 7; pp. 1564-1583.

Otsuka K. and Wayman C. M.; "Shape Memory Materials"; First Edition; Cambridge University Press; Cambridge, UK; 1998.

Pharr G. M.; "Measurement of Mechanical Properties by Ultra-low Load Indentation"; *MATERIALS SCIENCE AND ENGINEERING A*; 1998; vol. A295; pp. 151-159. G. M. Pharr

Sehitoglu H., Anderson R., Karaman I., Gall K., and Y. Chumlyakov; "Cyclic Deformation Behavior of Single Crystal NiTi"; In Press *MATERIALS SCIENCE AND ENGINEERING A*; 2001.

Sehitoglu H., Karaman I., Anderson R., Zhang X., Gall K., Maier H.J., and Chumlyakov Y.; "Compressive response of NiTi single crystals"; *ACTA MATERIALIA*; 2000; Vol. 48: (13) 3311-3326.

Stelmashenko N. A., Walls M. G., Brown L. M., and Milman Y. V.; "Microindentation on W and Mo Oriented Single Crystals: An STM Study" ; *ACTA METALLURGICAL ET MATERIALIA*; 1993; vol. 41; pp. 2855-2865.

Stelmashenko N. A. and Brown L. M.; "Deformation structure of microindentations in W(100): A TEM study"; *PHILOSOPHY MAGAZINE A*; 1996; vol. 74; pp. 1195-1206.

Surikova N. S. and Chumlyakov Y. I.; "The Peculiarities of Deformation and Fracture of Hardened Titanium Nickelide"; *PHYSICAL MESOMECHANICS*; 2000; Vol. 1; pp. 93-102.

Tanaka K., Kanari M., and Matsui N.; "Continuum dislocation model of Vickers indentation on a zirconia"; *ACTA MATERIALIA*; 1999; vol. 47; pp. 2243-2257.

Treppman D., Hornbogen E., and Wurzel D.; "The effect of combined recrystallization and precipitation processes on the functional and structural properties in NiTi alloys"; *JOURNAL DE PHYSIQUE IV*; 1995; Vol. 5: (C8) 569-574.

AD NUMBER	DATE 13 AUG 01	DTIC ACCESSION NOTICE
1. REPORT IDENTIFYING INFORMATION		REQUE: 1. Put you on rever 2. Complet 3. Attach fc mailed 4. Use unc informa 5. Do not c for 6 to
A. ORIGINATING AGENCY NAVAL POSTGRADUATE SCHOOL, MONTEREY, CA 93943		
B. REPORT TITLE AND/OR NUMBER EFFECTS OF PRECIPITATE SIZE AND SURFACE NORMAL		
C. MONITOR REPORT NUMBER BY KEVIN K. JUNTUNEN, UNIV OF COLORADO		
D. PREPARED UNDER CONTRACT NUMBER N62271-97-G-0051		
2. DISTRIBUTION STATEMENT APPROVED FOR PUBLIC RELEASE: UNLIMITED DISTRIBUTION		DTIC: 1. Assign A 2. Return

DTIC Form 50
JUL 96

PREVIOUS EDITIONS ARE OBSOLETE